Draft version April 3, 2024
Typeset using LaTeX **twocolumn** style in AASTeX631

Haro 11: The Spatially Resolved Lyman Continuum Sources

Lena Komarova [1], M. S. Oey [1], Svea Hernandez [2], Angela Adamo [3], Mattia Sirressi [3], Claus Leitherer [2], J. M. Mas-Hesse [4], Göran Östlin [3], Edmund Hodges-Kluck [5], Arjan Bik [3], Matthew J. Hayes [3], Anne E. Jaskot [6], Daniel Kunth [7], Peter Laursen [8,9], Jens Melinder [3], and T. Emil Rivera-Thorsen [3]

[1] *Astronomy Department, University of Michigan, 1085 South University Avenue, Ann Arbor, MI 48109, USA*
[2] *AURA for ESA, Space Telescope Science Institute, 3700 San Martin Drive, Baltimore, MD 21218, USA*
[3] *Department of Astronomy, Oskar Klein Centre, Stockholm University, AlbaNova University Centre, SE-106 91 Stockholm, Sweden*
[4] *Centro de Astrobiología – Dept. de Astrofísica (CSIC-INTA), 28850 Madrid, Spain*
[5] *NASA Goddard Space Flight Center, Greenbelt, MD 20771, USA*
[6] *Astronomy Department, Williams College, Williamstown, MA 01267, USA*
[7] *Institut d'Astrophysique, Paris, 98 bis Boulevard Arago, F-75014 Paris, France*
[8] *Cosmic Dawn Center (DAWN)*
[9] *Niels Bohr Institute, University of Copenhagen, Jagtvej 128, DK-2200, Copenhagen N, Denmark*

(Accepted March 31, 2024)

ABSTRACT

As the nearest confirmed Lyman continuum (LyC) emitter, Haro 11 is an exceptional laboratory for studying LyC escape processes crucial to cosmic reionization. Our new HST/COS G130M/1055 observations of its three star-forming knots now reveal that the observed LyC originates in Knots B and C, with 903−912 Å luminosities of $1.9\pm1.5\times10^{40}$ erg s^{-1} and $0.9\pm0.7\times10^{40}$ erg s^{-1}, respectively. We derive local escape fractions $f_{\rm esc,912} = 3.4\pm2.9\%$ and $5.1\pm4.3\%$ for Knots B and C, respectively. Our Starburst99 modeling shows dominant populations on the order of $\sim 1-4$ Myr and $1-2\times10^7$ M$_\odot$ in each knot, with the youngest population in Knot B. Thus, the knot with the strongest LyC detection has the highest LyC production. However, LyC escape is likely less efficient in Knot B than in Knot C due to higher neutral gas covering. Our results therefore stress the importance of the intrinsic ionizing luminosity, and not just the escape fraction, for LyC detection. Similarly, the Lyα escape fraction does not consistently correlate with LyC flux, nor do narrow Lyα red peaks. High observed Lyα luminosity and low Lyα peak velocity separation, however, do correlate with higher LyC escape. Another insight comes from the undetected Knot A, which drives the Green Pea properties of Haro 11. Its density-bounded conditions suggest highly anisotropic LyC escape. Finally, both of the LyC-leaking Knots, B and C, host ultra-luminous X-ray sources (ULXs). While stars strongly dominate over the ULXs in LyC emission, this intriguing coincidence underscores the importance of unveiling the role of accretors in LyC escape and reionization.

Keywords: Lyman-alpha galaxies (978) — Starburst galaxies (1570) — Massive stars (732) — Young massive clusters (2049) — Stellar feedback (1602) — H II regions (694) — Dwarf irregular galaxies (417) — Radiative transfer (1335) — Intergalactic medium (813) — Ultraluminous X-ray sources (2164)

1. INTRODUCTION

The ionizing sources and physical mechanisms responsible for cosmic reionization at z > 6 remain a critical unsolved problem in cosmology. The major contenders for providing the required LyC are active galactic nuclei (AGN) and massive stars in starbursts, with their relative contributions to reionization still uncertain. Ac-

Corresponding author: Lena Komarova
komarova@umich.edu

creting sources other than AGN, e.g. ultra luminous X-ray sources (ULXs), may also play a significant role in ionizing the IGM (Madau & Fragos 2017; Ross et al. 2017; Sazonov & Khabibullin 2018). Some studies show that AGN could produce sufficient energy to reionize the universe (e.g., Madau & Haardt 2015; Giallongo et al. 2015); while others suggest that the AGN number density and ionizing emissivity were too low in the early universe (Shankar & Mathur 2007; Fontanot et al. 2012; Hassan et al. 2018; Faucher-Giguère 2020), pointing to star-forming galaxies as the dominant source. On the other hand, while dwarf starbursts seem to be promising candidates for reionization agents (Bouwens et al. 2012; Sharma et al. 2017; Yeh et al. 2023), they may not have sufficiently high escape fractions (e.g., Fontanot et al. 2014). JWST is now revealing the blue UV slopes of the earliest, $z = 8-16$, galaxies, pointing to young and dust-poor stellar populations (Cullen et al. 2023a,b; Topping et al. 2023; Morales et al. 2023), in further support of galaxy-driven reionization. JWST is moreover uncovering an abundance of high-redshift starbursts with high ionizing photon production efficiencies, implying that galaxies could have reionized the universe with somewhat lower escape fractions than previously assumed (Matthee et al. 2023; Atek et al. 2024).

Knowing the relevant UV sources is only half of the problem, however. The other key question is how LyC escapes the immediate environment of the source without being absorbed by the local interstellar medium (ISM). The standard paradigm for stellar-driven reionization is that supernovae and stellar winds clear pathways in the ISM that become optically thin to LyC (e.g., Clarke & Oey 2002; Fujita et al. 2003; Ma et al. 2016). There is now evidence of a radiation-driven feedback mode that also may enable LyC escape in the most extreme metal-poor starbursts such as extreme Green Peas (GPs) (Jaskot et al. 2017; Komarova et al. 2021; Flury et al. 2022a,b). Similarly, accretion-driven sources such as AGN or X-ray binaries may create optically thin channels through winds and jets (Smith et al. 2020).

Haro 11 is an extreme dwarf starburst galaxy with dozens of young massive clusters (Adamo et al. 2010; Sirressi et al. 2022) and a gas consumption timescale of 50 Myr (Östlin et al. 2021). It is one of the most important local ($z = 0.021$) galaxies for advancing our understanding of cosmic reionization, and a wealth of data across the electromagnetic spectrum exist for this object. Haro 11 is the first local Lyman continuum emitter (LCE) to be observationally confirmed (Bergvall et al. 2006; Leitet et al. 2011), and is moreover the closest one, lying at a distance of only 88.5 Mpc (assuming $H_0 = 73$ km s^{-1} Mpc^{-1}; Sirressi et al. 2022, hereafter S22). With its intense star formation triggered by a dwarf galaxy merger (e.g., Östlin et al. 2001, 2015), Haro 11 is dominated by three starburst knots: A, B, and C (Kunth et al. 2003), indicated in Figure 1. While Knot A is a purely star-forming region, with properties consistent with those of Green Peas (Keenan et al. 2017), Knots B and C host ULXs (Prestwich et al. 2015), including a possible low-luminosity AGN (LLAGN) (Gross et al. 2021). Thus, Haro 11 is a prime laboratory for pinpointing the nature of UV sources and LyC escape processes crucial to reionization.

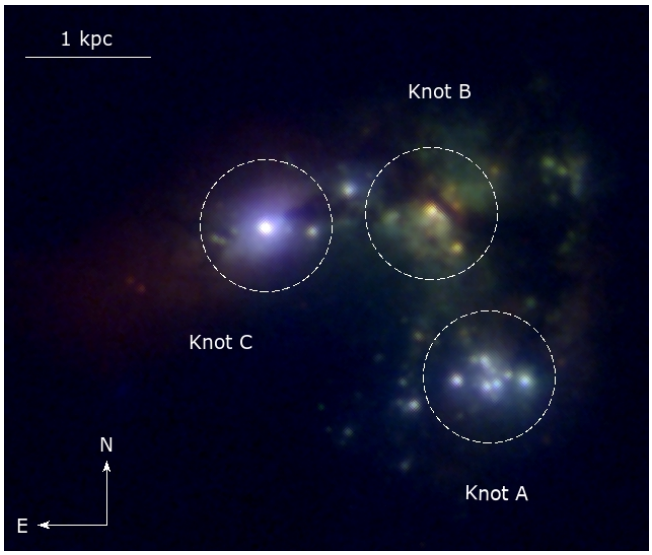

Figure 1. HST color composite image of Haro 11, indicating Knots A, B, and C, as well as the COS apertures (red = 5500 Å continuum, F550M; green = 3360 Å continuum, F336W; blue = Lyα, F122M).

However, the initial LyC detection (Bergvall et al. 2006) did not resolve which of the three knots is/are responsible for the LyC emission, since the $30'' \times 30''$ FUSE aperture encompassed the entirety of the galaxy. Unveiling the exact source(s) of the Haro 11 LyC leakage is necesssary to clarify the relative roles of compact objects and massive stars in this prototypical object. The three knots vary drastically in Lyα emission properties, extinction, stellar populations, and gas properties. So, putting the LyC detection in context of knot properties reveals the connection between environment and LyC escape. In this paper, we present HST/COS observations of the three knots at wavelengths below the Lyman limit, revealing the LyC-emitting sources. Section 2 contains the details of observations and data analysis. We present our results in Section 3, discuss cosmological implications in Section 4, and summarize our main conclusions in Section 5.

2. OBSERVATIONS AND ANALYSIS

We obtained HST/COS FUV spectra of Knots A, B, and C in Haro 11 (Cycle 28, program ID 16260, PI: Oey). We used the medium-resolution G130M grating in TIME-TAG mode, coupled with the 2.5″ Primary Science Aperture (PSA), with all four grating offset positions (FP-POS = ALL). The observations were taken with the grating centered on 1055 Å, and resolving power $R \sim 10,000$. A total of 13 Visits over the course of 24 orbits were obtained, in 2021 January, May, October, November, and December; and 2022 May and July. For each Visit on each knot, we obtained 4 sub-exposures at different focal plane offset positions in the wavelength range 900 – 1200 Å. Some sub-exposures had unusable data due to acquisition failures and resulted in additional Visits. All sub-exposures used for the LyC measurements are listed in Table 1.

The raw COS observations were calibrated with `CalCOS` version 3.4.0 (Soderblom 2021). Given that the observations for the individual knots were obtained throughout several different Visits, with more than one association file, we combined their individual calibrated `x1d` files using the `IDL` software by Danforth et al. (2010, 2016). We combined the spectra, weighting by exposure times and taking into account the data quality (DQ) flags set by the standard `CalCOS` pipeline.

A critical step in the calibration of Lyman continuum observations is an accurate background correction. The standard `CalCOS` pipeline estimates the background contribution in the region of the detector where the science spectrum is located, by computing the average counts in two predefined regions external to the science extraction region. For the COS FUV detector, these two predefined regions are typically located below and above the science extraction box, depending on the lifetime position (LP) used at the time of the observations. The COS team has reported that the background levels are correlated with solar activity (Dashtamirova et al. 2019), detector gain and high voltage (HV). Additionally, they have found that the background levels vary throughout the detector and with time, with slightly higher levels towards the edge of the detector.

To investigate whether the background correction was accurately accounting for the expected detector contribution in the science extraction regions, we collapsed the 2-dimensional `flt` images in the dispersion direction. For the G130M/1055 configuration observed at Lifetime Position 2, the background region boundaries are located at pixels $y \sim 448$ and $y \sim 728$, with predefined widths of 51 pixels. Inspection of the collapsed profiles showed that in all exposures the background region centered on pixel $y \sim 728$ showed a slightly higher background level towards the edge of the detector than that observed closer to the science extraction region. This in turn caused a slight oversubtraction of the science spectra. To improve the background correction, we modified the location of the background regions in the extraction tab reference file (`XTRACTAB`) to be closer to the science extraction region (centered at $y \sim 588$), centering the predefined regions around pixels $y \sim 505$ and $y \sim 663$. The background estimates using these new regions were $\sim 3-6\%$ lower than those calculated at the original background locations.

Given the extended nature of the Haro 11 targets, we adopted a `BOXCAR` extraction technique, available in `CalCOS`. As detailed in James et al. (2022), for extended targets, a broader extraction box may be necessary to collect the full extent of their flux. To select an optimal extraction height value for the science region, we explored varying the nominal size by ±8 pixels, in steps of 2 pixels, aiming to improve the signal-to-noise of the extracted spectrum. We adopted extraction heights for the science regions in COS segment B of 63 (standard), 71, and 71 pixels for Knots A, B, and C, respectively.

We sum the high-quality spectra from each Visit on each knot, with total effective exposure times for Knots A, B, and C of 4.7, 4.0, and 3.3 hours, respectively (Table 1). To maximize the signal-to-noise ratio, we more-

Table 1. COS G130M/1055 Observations

Target	UT Start Date	Exposure time [a] (s)
Knot A	2021-05-06	2,672
	2021-05-07	3,406
	2021-10-13	2,306
	2021-12-01	2,306
	2021-12-01	3,862
	2022-05-20	2,306
		Total: 16,858
Knot B	2022-05-20	4,924
	2022-07-05	4,712
	2022-07-07	4,713
		Total: 14,349
Knot C	2021-01-27	4,841
	2021-05-12	3,500
	2021-01-25	4,847
	2021-12-01	2,306
		Total: 11,994

Notes.

[a] Exposure times used in all Visits incorporated in our LyC measurements.

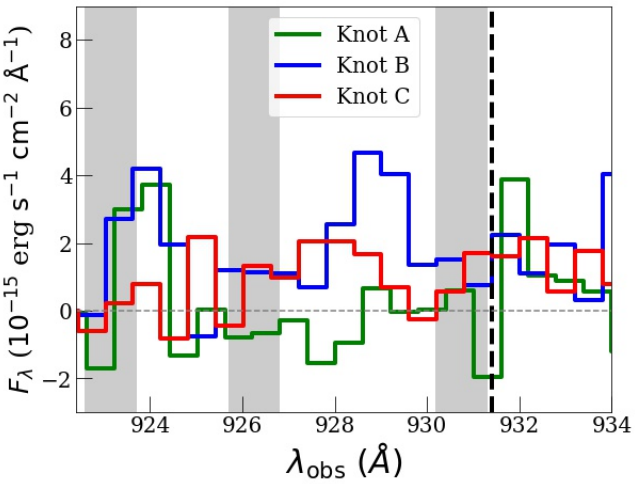

Figure 2. New HST/COS Lyman continuum observations of Knots A, B, and C in Haro 11. We measure the LyC in a 9 Å window between 922.4 Å (the left edge of the figure) and the redshifted Lyman limit at 931.4 Å, shown as a black dashed line. The gray regions represent intervals that were excluded from LyC measurements due to geocoronal emission lines.

over bin the spectra by 6 G130M/1055 resolution elements, and thus 60 pixels ≈ 0.6 Å.

Our reduced, median-combined COS LyC spectra for the three knots are shown in Figure 2. The LyC region we observe is a 9 Å window below the redshifted Haro 11 Lyman limit of 931.4 Å, as indicated in Figure 2. We compute the mean LyC flux densities F_{912} in the three knots, excluding 1.1 Å-wide geocoronal H Lyman series line regions at 930.75 Å, 923.15 Å, and 926.25 Å. The flux measurement remains the same within the error, when including these regions. There are no other known geocoronal features within the measured region. Our observed LyC fluxes and luminosities are shown in Table 2. We detect the strongest LyC emission in Knot B, which has about 2/3 of the total flux, leaving 1/3 in Knot C and none in Knot A. Our combined LyC flux density from Knots B and C is $F_{912} = (3.5 \pm 2) \times 10^{-15}$ erg s^{-1} cm^{-2} Å^{-1}, consistent with the $(4.0 \pm 0.9) \times 10^{-15}$ erg s^{-1} cm^{-2} Å^{-1} measured by Leitet et al. (2011) in the $30'' \times 30''$ FUSE aperture.

3. STELLAR POPULATIONS AND LYC ESCAPE

To quantify the LyC escape efficiency in each region, we compute the local escape fraction as:

$$f_{esc,912} = \frac{L_{912,obs}}{L_{912,int}} \quad , \qquad (1)$$

where $L_{912,obs}$ is the observed integrated luminosity in our 9 Å window of 903 – 912 Å at rest (or 922 – 931 Å in the Haro 11 frame), and $L_{912,int}$ is the intrinsic luminosity in this range, similar to Leitet et al. (2011). Thus, $f_{esc,912}$ is an approximation for the fraction of the total produced ionizing power that escapes the region. We assume that the ionizing luminosity is dominated by FUV radiation from massive stars, and we estimate $L_{912,int}$ by modeling the stellar population in each knot as described below.

Sirressi et al. (2022) have previously constrained the stellar populations of Haro 11 using multi-band HST photometry in the F140LP, F220W, F275W, F336W, F435W, F550M, F555W, F665N, and F814W filters (Östlin et al. 2009; Adamo et al. 2010). Fitting the resulting SEDs, they estimate individual cluster parameters in each knot. They additionally use FUV $1150 - 1800$ Å COS G130M/1300 + G160M/1600 spectra (Östlin et al. 2021, programs 15352, 13017; PIs Östlin, Heckman) and optical $4650 - 7000$ Å MUSE spectra (Menacho et al. 2019, program 096.B-0923(A); PI Östlin). The G130M/1300 spectra were corrected for broad Lyα absorption as described in Sirressi et al. (2022). As detailed in Menacho et al. (2019), the MUSE observations of each knot are the result of 16 dithered integrations at 4 different position angles. The final MUSE spectra were extracted with apertures of the same size as for the COS spectra, 2.5″ in diameter, and corrected for vignetting, with the resulting FUV and optical continua well matched across the wavelength gap.

We combine these existing spectroscopic observations with our newly obtained COS G130M/1055 spectra ($900 - 1200$ Å) to model each knot's stellar content. To increase the signal-to-noise in the UV, we further bin all COS spectra by a factor of 2 in wavelength and median-combine the overlap region. Since the G130M/1055 spectra have different initial extracted spectral sampling from the G130M/1300 and G160M/1600 data (0.6 and 0.4 Å px^{-1}, respectively), the final combined UV spectrum has sampling of 1.2 and 0.8 Å px^{-1}, over the respective ranges, while the optical MUSE data sampling is 1.2 Å px^{-1}. The combined spectra of the three knots are shown in Figures 3 – 5. Below we describe our stellar population modeling assumptions, spectral features of interest, and fitting procedure.

We use Starburst99 (Leitherer et al. 1999, 2014) model spectra of varying cluster ages ($1 - 100$ Myr), masses ($10^5 - 10^9$ M$_\odot$), and extinctions ($E(B-V) = 0$ to 1). We also consider different star formation histories, specifically, constant star formation (CSF) or single stellar populations (SSPs). We fit either CSF or a maximum of 3 SSPs to each knot's combined COS G130M/1055 + G130M/1300 + G160M/1600 + MUSE spectrum. While the S22 photometric analysis revealed

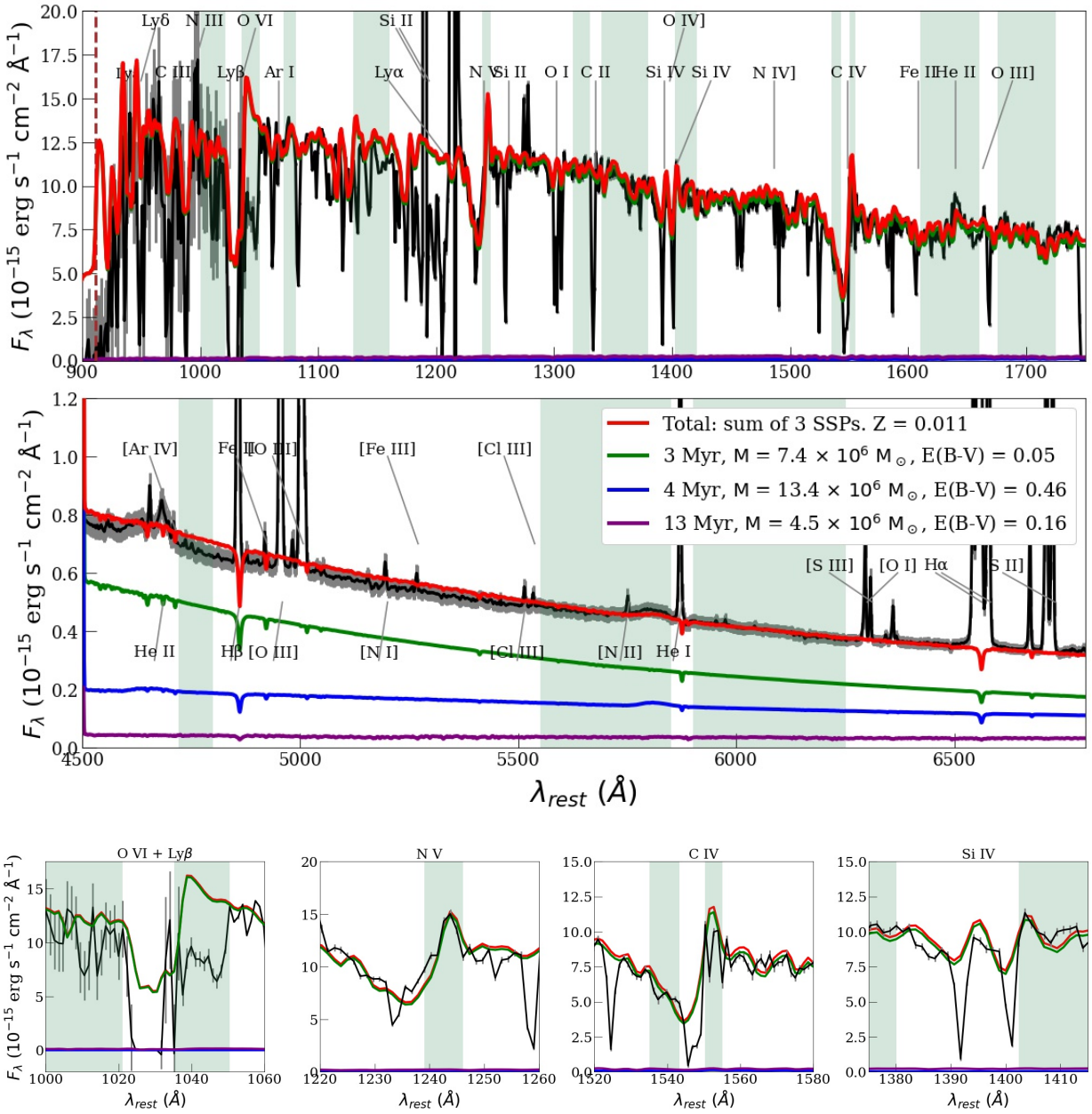

Figure 3. Top: Combined new COS G130M/1055 + Sirressi et al. (2022) G130M/1300 + G160M/1600 + MUSE observations (black) of Haro 11 Knot A, and our model consisting of 3 SSPs, indicated by the colored lines as shown. The light green regions represent intervals that were used for fitting the models to the data. The rest was excluded to mask ISM and nebular lines, geocoronal emission, and detector gaps. Bottom: Zoom of age-sensitive O VI, N V, C IV, and Si IV P-Cygni profile fits.

at least 7 individual star clusters in each knot, our goal is to approximate the $1-3$ dominant stellar populations within each region. We evaluate a number of stellar model assumptions by using a variety of evolutionary tracks. With respect to S22, we extend the parameter space to include stellar rotation, testing Geneva 2012 tracks with $v = 0$, $v = 0.4 \times v_{\rm breakup}$ (Ekström et al. 2012a). We also consider standard or high mass loss: Ekström et al. (2012a) or Meynet et al. (1994) tracks. For all models, a Salpeter initial mass function (IMF) with stellar mass range $0.1 - 120$ M$_\odot$ is assumed, similarly to S22. The stellar mass normalizations depend on the low-mass end of the IMF, and we estimate that our resulting masses would be 1.6× lower if a Kroupa IMF had been assumed. We re-sample the model spectra onto our observed wavelength grid, matching the vari-

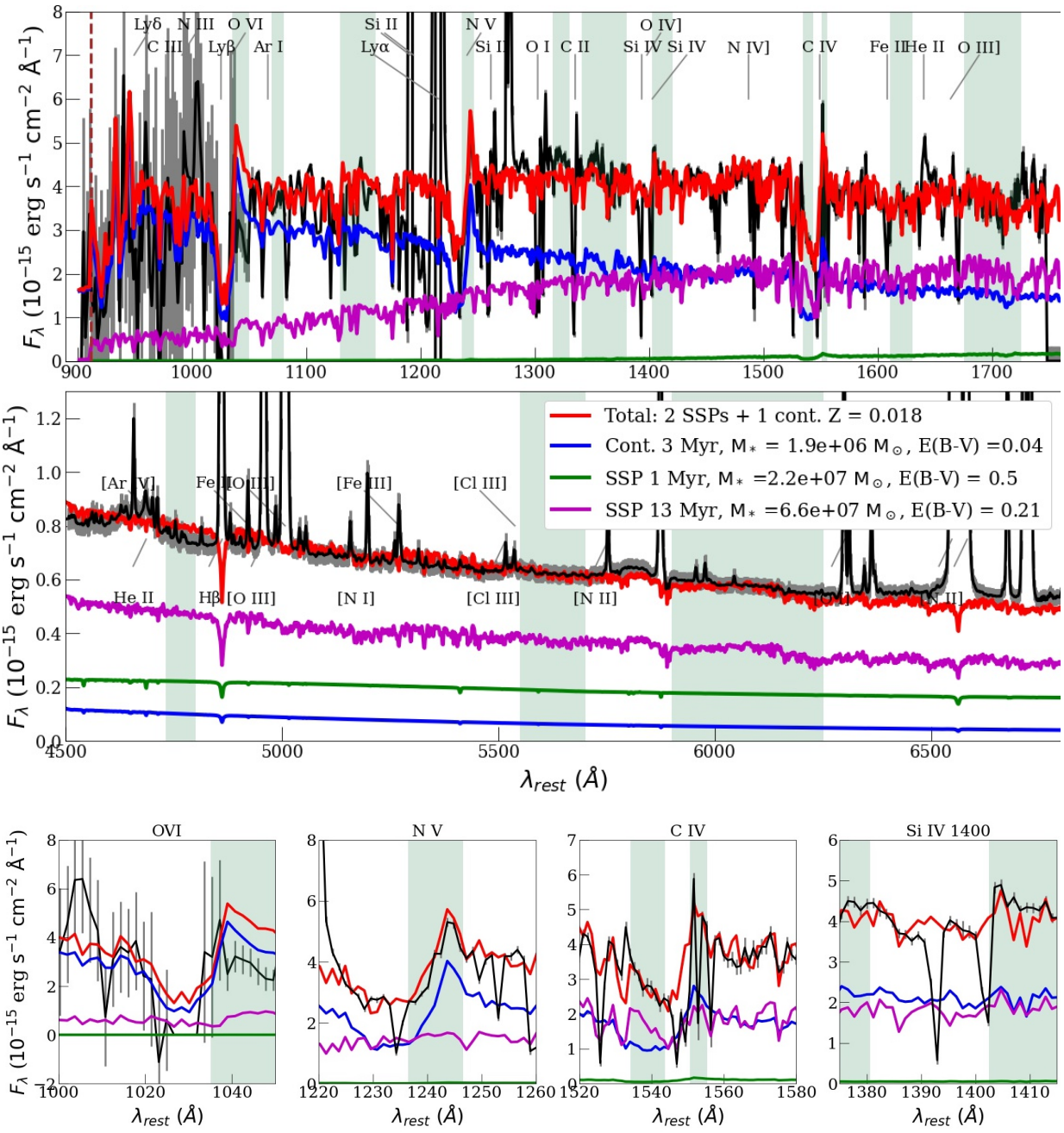

Figure 4. Same as Figure 3 but for Knot B. The model assumes two single stellar populations and an episode of continuous star formation.

able sampling, and convolve with a Gaussian of width ~ 1 Å, equal to the stellar broadening we measure from photospheric C III 1247.

Following S22, we perform a linear interpolation of the model spectra between the discrete metallicity values available in Starburst99 ($Z = 0.001, 0.008, 0.02$), in order to estimate models for metallicities appropriate to Haro 11. Previous Haro 11 metallicity measurements have yielded discrepant results spanning a factor of two in each knot (Guseva et al. 2012; James et al. 2013; Menacho et al. 2021). Menacho et al. (2021) provide a comprehensive summary and discussion of the previous metallicity measurements. While these measurements relied on the same, direct method, the discrepancies are attributed to differences in ionization correction factors and aperture sizes, as well as some possible real varia-

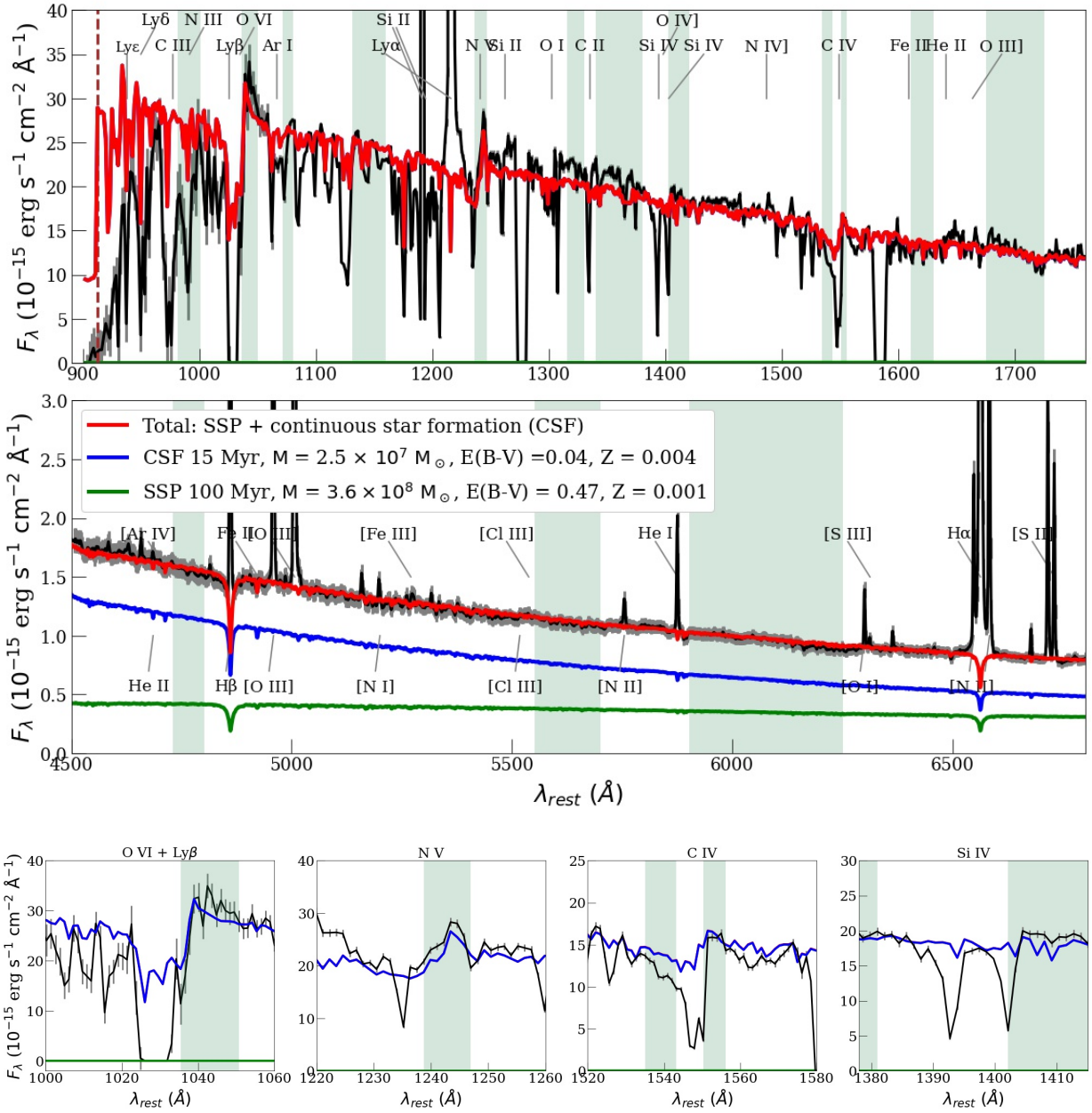

Figure 5. Same as Figure 3 but for Knot C. The model assumes one episode of continuous star formation plus an older background population (see text).

tions between stellar and ionized gas metallicities probed by different apertures. We therefore use the most spatially resolved metallicity measurements for Haro 11 by Menacho et al. (2021), adopting their measured central values for Knots A and B. For Knot C, which shows a much larger age spread, 1 − 100 Myr, we treat metallicity as a free parameter and obtain values consistent with Menacho et al. (2021). Lastly, we apply extinction to the models, using the SMC law from Prevot et al. (1984). If the Calzetti et al. (2000) law is assumed, it again results in unreasonably high extinctions compared to previous measurements, and thus also stellar masses.

Since our objective is to constrain the youngest, LyC-emitting population, we focus on fitting the age-sensitive O VI λ1038, N V λ1243, C IV λ1548, and Si IV λ1400 P Cygni features, which trace stellar winds from young stars, as well as the optical and UV continuum, which helps constrain the extinctions and mass normalizations. While we do not weigh the P Cygni profiles differently in fitting the spectrum, we reject models that fit the

Table 2. LyC Fluxes and Observationally Derived Properties of Knots A, B, and C.

Parameter	Knot A	Knot B	Knot C	Reference
F_{912} (10^{-15} erg s^{-1}cm^{-2} Å^{-1})	< 3.35	2.31 ± 1.8	1.20 ± 0.94	1
$L_{912,\rm obs}$ (10^{40} erg s^{-1})	< 2.82	1.95 ± 1.5	0.92 ± 0.72	1
12 + log(O/H)	8.42 ± 0.02	8.64 ± 0.02	7.64 ± 0.01	2
O_{32}	9	8	1	7
Q_0(Hα)[a] (10^{53} s^{-1})	2.3 ± 0.1	8.2 ± 0.4	2.3 ± 0.1	4
$f_{\rm c,Si\ II}$	0.95 ± 0.05	0.96 ± 0.04	0.55 ± 0.05	6
$f_{\rm c,HI}$	~ 1	~ 1	~ 0.8	6
log($N_{\rm Si\ II}$/cm^{-2})	15.2 ± 0.3[b]	15.3 ± 0.3	14.7 ± 0.3	6
log($N_{\rm HI}$/cm^{-2})	20.7 ± 0.1[b]	21.0 ± 0.1	–	6
$L_{\rm Ly\alpha}$ (10^{40} erg s^{-1})	3.2 ± 0.3	6.1 ± 0.6	14.0 ± 1.4	6
$f_{\rm esc,Ly\alpha}$	$1.2 \pm 0.1\%$	$0.65 \pm 0.06\%$	$5.9 \pm 0.6\%$	6
$v_{\rm sep,Ly\alpha}$ (km s^{-1})	532 ± 20	409 ± 20	400 ± 20	6
$L_{\rm X}$ [0.3-8 keV] (10^{40} erg s^{-1})	–	9.5 ± 1	4.5 ± 1	5

[a] The emission rate of H-ionizing photons, derived from the de-reddened Hα luminosity.

[b] We estimate the errors on the published column densities from other measurements in the study, but the uncertainties are poorly constrained due to asymmetric confidence intervals.

References—(1) This work; (2) Menacho et al. (2021); (3) James et al. (2013); (4) Sirressi et al. (2022); (5) Gross et al. (2021); (6) Östlin et al. (2021); (7) Keenan et al. (2017); (8) Menacho et al. (2019)

continuum but not the P Cygni features. We mask out the narrow interstellar absorption components before fitting, taking special care in the absorption regions of P Cygni lines. We further isolate feature-free sections of the UV and optical continuum, and mask out nebular emission lines, ISM features, and detector gaps before fitting. The spectral regions we use for fitting are shown in the green sections in Figures 3 – 5. We note that O VI λ1038 has contamination from Lyβ and moreover, the stellar wind feature in the model atmospheres is especially uncertain due to combined effects of wind inhomogeneities and X-rays, as well as low signal-to-noise. For each knot's spectrum, discrete age combinations from 1 to 100 Myr are fit in steps of 1 Myr, determining the best-fitting masses and extinctions using the differential evolution minimizer in the Python package `lmfit`. The best model is then chosen as the age, stellar mass M, and extinction $E(B-V)$ combination that results in the lowest χ^2.

Testing the effects of stellar rotation and assumed mass loss rates, we find that, for all three knots, the evolutionary tracks that produce the highest-quality fits are high mass-loss, non-rotating 1994 Geneva models (Meynet et al. 1994). In these tracks, the mass-loss rate was doubled from the "standard" case (Schaerer et al. 1993), to match observations. Since 2012, a lower, theoretical mass-loss prescription (Vink et al. 2001) has been adopted by the Geneva group accounting for wind inhomogeneities, based on clumping-corrected mass-loss rates (Ekström et al. 2012b; Georgy et al. 2013). Models assuming the opposite cases of fast rotation and low mass-loss produce reasonable fits for Haro 11, but with consistently higher χ^2 values. The preference for non-rotating tracks in Haro 11 suggests the rotation rates to be at the slower end of the spectrum defined by the two available rates of $v = 0$ and $v = 0.4 \times v_{\rm breakup}$. Noting that mass loss and rotation rates require further study in low-metallicity systems, we present the stellar population fits assuming high mass-loss and zero rotation, similarly to S22.

For each knot's stellar population fit, we compute $L_{912,\rm int}$ from the model spectrum and obtain the escape fraction from equation 1. For the escape fraction uncertainty, we combine the error in the detected LyC luminosity with that in the modelled $L_{912,\rm int}$, which we obtain by Monte Carlo sampling our best-fit stellar masses and ages 10^4 times. We also calculate the predicted Q_0, the emission rate of H-ionizing photons, to compare to that inferred from Hα observations, Q_0(Hα). The latter was measured for all knots by Sirressi et al. (2022)

from the MUSE spectra, extracted with the same apertures as in the FUV COS observations. HST/WFC3 F665N imaging suggests that $Q_0(\mathrm{H}\alpha)$ is underestimated by 25%, 15%, and 15% for Knots A, B, and C, respectively. We also estimate the predicted thermal FIR luminosity of each knot that arises from dust-processed optical and UV radiation, by integrating the difference between the intrinsic and the reddened model spectra in our fitting ranges $912-1750$ Å and $4500-7000$ Å. To compare to observations, we derive the $1-1000$ μm luminosity from the galaxy-integrated *IRAS* $F_{60\mu\mathrm{m}}$, $F_{100\mu\mathrm{m}}$ fluxes and the Helou et al. (1988) prescription, obtaining $L_{\mathrm{FIR}} = 2.7 \pm 1.3 \times 10^{44}$ erg s^{-1}. So, the dust content in Haro 11 generates a substantial FIR luminosity consistent with luminous infrared galaxies (LIRGs). This value is reasonably consistent with the sum of our estimated FIR luminosities from the individual knots obtained below, which is 1.7×10^{44} erg s^{-1}.

Detailed stellar population fits for each knot are presented below, with resulting parameters shown in Table 3, together with a discussion of the LyC escape efficiency and mechanisms. We present our results for the three knots in order of decreasing detected LyC flux.

3.1. *Knot B*

We find that the region of Haro 11 with the brightest measured LyC is Knot B. Using the distance of 88.5 Mpc to Haro 11, we obtain $L_{912,\mathrm{obs}} = (2 \pm 1.5) \times 10^{40}$ erg s^{-1} for Knot B (Table 2). This region by far dominates the Hα emission of Haro 11 and thus has the highest intrinsic ionizing power among the three knots, with $Q_0(\mathrm{H}\alpha) = 8 \times 10^{53}$ s^{-1} (Sirressi et al. 2022). Its young massive stars should therefore dominate the production of ionizing photons in Haro 11. However, this object shows large amounts of gas and dust, and it therefore has been somewhat overlooked in the literature when considering the origin of the LyC from this galaxy.

Our stellar population synthesis confirms that Knot B produces the most ionizing radiation in Haro 11. The best-fitting model for the combined COS G130M/1055 + G130M/1300 + G160M/1600 + MUSE spectrum of Knot B is shown in Figure 4. A strong match for the spectrum (reduced $\chi^2 = 1.7$), with age-sensitive P-Cygni wind features well fitted, consists of a continuous star formation episode for the last 3 Myr, as well as 1-Myr and 13-Myr single stellar populations. The 1 Myr component is the youngest age observed in Haro 11, as can be seen in Table 3, where detailed stellar population model parameters are shown for all knots. Moreover, Knot B has the most massive LyC-bright population, where the stellar mass in ages < 5 Myr is 2.4×10^7 M$_\odot$, which is 3$\times$ higher than that found in the second-brightest LyC-leaking region, Knot C. As shown in Table 3, Knot B thus has the highest ionizing photon production efficiency among the knots, $\log(\xi_{\mathrm{ion}}) = 25.3$, compared to 25.2 in Knots A and C. Notably, the dominant, 1-Myr component in Knot B is heavily obscured, showing $E(B-V) = 0.5$ and contributing marginally to the observed FUV flux. The age-sensitive P Cygni features are thus accounted for by the 3 Myr CSF component alone, while the dusty 1 Myr component contributes $\sim 30\%$ of the optical luminosity. But with a mass of $\sim 2 \times 10^7$ M$_\odot$, the 1 Myr population successfully reproduces the high photoionization rate inferred from Hα. As can be seen in Tables 2 and 3, our model gives a total $Q_0 = 1 \times 10^{54}$ s^{-1}, while that inferred from Hα is $Q_0(\mathrm{H}\alpha) = 0.8 \times 10^{54}$ s^{-1}, which is in good agreement. Our predicted FIR luminosity, dominated by the 1-Myr component and tracing dust-processed radiation, is $L_{\mathrm{FIR}} = 1.3 \times 10^{44}$ ergs^{-1}. Our modeling thus confirms the existence of a massive, obscured young population that dominates the ionizing power and FIR luminosity of Knot B.

Our results can be compared to the S22 photometrically derived cluster parameters given in Table 4. S22 photometric modelling pointed to 10 clusters within the COS aperture with ages 1–5 Myr of varying masses and extinctions, as well as a 14 Myr cluster. Since we fix the number of separate population components in our spectroscopic analysis to three, our model for Knot B cannot account for all the S22 cluster ages. But our model is consistent with the two youngest S22 clusters, 1 Myr and 2 Myr, where our total mass in these ages is within 40% of the corresponding mass found by S22, and we find similarly high extinctions of $E(B-V) \sim 0.5$. Notably, while Wolf-Rayet (WR) emission features (e.g., He I λ1640, and the λ5608 Å and λ4650 Å bumps) are not included in Starburst99 models, these features observed in the spectrum of Knot B are signatures of a $\gtrsim$3 Myr population, consistent with the presence of photometrically derived 4 Myr old clusters (Table 4). Our 3-Myr CSF component thus accounts both for the presence of the youngest stars, as well as the more evolved WR components. Lastly, the 13 Myr component we find is 40$\times$ more massive than the 14 Myr cluster, which may be attributed to the spectroscopic aperture also capturing the extended, diffuse populations.

Given the large cluster masses and young ages seen in Knot B, it could feasibly host Very Massive Stars (VMS, M $>$ 120 M$_\odot$). We examine the spectrum of Knot B for VMS diagnostics, such as O V λ1371 absorption,

Table 3. Parameters Fitted from Spectroscopic Stellar Population Models

Region	Model[a]	Age	M	$E(B-V)$	Z[b]	$L_{\rm FIR}$	Q_0	$\log(\xi_{\rm ion})$	$f_{\rm esc,912}$
		Myr	10^6 M$_\odot$			10^{43} erg s^{-1}	10^{53} s^{-1}	Hz erg^{-1}	
		3±0.5	7.4±0.6	0.05±0.01		0.8	2.3		
Knot A	3 SSPs	4±0.5	13.4±4.1	0.46±0.2	0.011	1.9	2.2	25.23	< 0.10
		13±3	4.5±1.2	0.16±0.05		0.1	3×10^{-3}		
	CSF	3±0.3	1.9±0.4	0.04±0.02		0.3	0.7		
Knot B	SSP	1±0.2	22±1.5	0.5±0.1	0.018	7.7	9.3	25.32	0.034±0.029
	SSP	13±2	66±10	0.21±0.06		4.7	0.02		
Knot C	CSF	15±3	26±4	0.04±0.01	0.004	1.1	4.0	25.22	0.051±0.043
	SSP	> 30[c]	360±80	0.47±0.25	0.001	0.7	2×10^{-4}		

Notes.

[a] Model for star formation: single stellar populations (SSPs) or continuous star formation (CSF).

[b] From Menacho et al. (2021).

[c] Fits based on both Starburst99 and Yggdrasil (see text). Ages up to ~ 2 Gyr can be fit.

Table 4. S22 Photometric Clusters

Region	Age	M	$E(B-V)$	$N_{\rm cl}$[a]
	Myr	10^6 M$_\odot$		
	4	1.4	0.06	1
Knot A	5	1.7	0.11	3
	6	3.3	0.06	3
	14	4.7	0.02	1
	15	10.8	0.07	3
	1	8.7	0.5	2
Knot B	2	7.2	0.4	1
	4	13.7	0.44	2
	5	44.1	0.4	4
	14	1.6	0.3	1
Knot C	6, 8 – 10	2.2	0.06	4
	15	44.3	0.05	3

Notes.

S22 cluster parameters combined in age bins, where masses are summed for the bin, and extinctions are averaged. The typical uncertainties on ages, masses, and extinctions are 1 Myr, 0.5×10^6 M$_\odot$, and 0.02, respectively. The metallicity fixed for the cluster analysis is $Z = 0.004$.

[a] $N_{\rm cl}$ is the number of clusters in each age bin.

He II λ1640 emission with equivalent width (EW) $>$ 3 Å, an absent or weak double-peaked red bump, and a blue bump without WR lines (Kunth & Sargent 1981; Martins et al. 2023; Wofford et al. 2023). We do not detect O V λ1371 in Knot B, and we measure its He II λ1640 EW to be 2.3 Å. The red bump detected in Knot B is broad and smooth, while the blue bump shows WR C IV λ4658. The above are all consistent with classical WR stars, and not VMS.

Although Knot B is the brightest LyC source in Haro 11, its local escape fraction is low. Based on the intrinsic LyC luminosity of our modelled stellar components, we obtain $f_{\rm esc,912}$= 0.034±0.029 (Table 3). The uncertainty is dominated by observational error of 77% on the detected flux, while the uncertainty in the intrinsic LyC luminosity is 21%. To compare to the escape fraction implied by the component cluster parameters, we model the clusters' UV spectra in Starburst99, based on their ages, masses, and metallicities. Summing their intrinsic LyC luminosities in the 903 – 912 Å range, we obtain $f_{\rm esc,912}= 0.02 \pm 0.01$ for the clusters, consistent with our spectroscopic model. Knot B also shows the lowest Lyα escape fraction among the three knots, $f_{\rm esc,Ly\alpha} = 0.65$ % (Östlin et al. 2021), although the observed Lyα peak separation of 400 km s^{-1} is similar to that observed in Knot C and other weak LyC leakers with $f_{\rm esc,LyC} \sim 0.03$ (Izotov et al. 2018; Flury et al. 2022b). The inefficiency of LyC and Lyα escape in Knot B can be explained by its significant gas and dust reservoir. It exhibits the highest H I column densities among the three knots, $\log(N_{\rm HI}/{\rm cm}^{-2}) \approx 21$ (Östlin et al. 2021), and the highest molecular gas mass, $M_{\rm H_2}$ = 2 x 10^9 M$_\odot$ (Gao et al. 2022). Moreover, it has a neutral covering fraction in Si II, $f_{\rm c,Si\ II} = 0.96$ (Östlin

et al. 2021) and thus $f_{c,HI} \geq 0.96$ in H I (Chisholm et al. 2018), consistent with the escape fraction we obtain. With filamentary dust clouds across the region further obscuring it, Knot B shows significant dust extinction of $E(B-V) = 0.5$ (Table 3).

Ionization-parameter mapping (IPM), on the other hand, points to a complex picture of optical depth. Knot B shows a significant [S II] $\lambda\lambda$6717,6731 deficiency, Δ[S II] $= -0.16$ (Östlin et al., in prep), where Δ[S II] is the displacement in log([S II]/Hα) from typical star-forming galaxies (Wang et al. 2021), which may indicate density-bounded conditions (Pellegrini et al. 2012; Wang et al. 2021). Values of [O II] λ3727/H$\alpha < 0.1$ indicate low optical depth, and for Knot B, [O II] λ3727/H$\alpha \sim$ 0.05 in the central line of sight (Keenan et al. 2017), suggests LyC escape. Knot B also shows elevated O_{32} = [O III] λ5007/[O II] λ3727 > 8 overall (Keenan et al. 2017), roughly twice the mean value observed in local unresolved LCEs (Flury et al. 2022a). Higher O_{32} values point to density-bounded conditions and correlate with the LyC escape fraction (Izotov et al. 2016a,b; Flury et al. 2022b). However, the extended region shows a confined, ionization-bounded morphology in transverse directions (Keenan et al. 2017). Therefore, Knot B must be leaking LyC through a narrow ionization cone in the line of sight. Menacho et al. (2019) report evidence of narrow highly ionized channels with Knot B at the base. They also find 1000 km/s outflows, likely driven by stellar feedback. We measure [S II]$\lambda\lambda$6716, 6731/H$\alpha = 0.14$ in our spectrum of Knot B, too low to signal shock heating by supernovae. The S22 photometrically derived cluster parameters in Knot B, the youngest of which we capture in our spectroscopic model, nevertheless imply a total power of 2×10^{41} erg/s in stellar winds and supernovae.

Since the LyC-leaking Knot B hosts an ultra-luminous X-ray source (ULX), its potential contribution to the LyC emission needs to be evaluated. This is an unusually bright, hard ULX (Prestwich et al. 2015). The X-ray emission has been revealed to originate from at least two objects (Gross et al. 2021). Based on the X-ray hardness, Gross et al. (2021) suggest that one or both of the sources is a black hole binary in a low-accretion, hard state, with the high X-ray luminosity suggesting the presence of an intermediate-mass black hole (IMBH) of mass $M_\bullet > 7600$ $M_\odot$ in the region. Alternatively, it may be a low-luminosity AGN (LLAGN), whose signatures are obscured by the dense gas and dust observed in Knot B or diluted by the intense star formation. It is thus possible for Knot B to be a unique merger site of two IMBH's or LLAGN (Gross et al. 2021).

However, we find that the ULX is unlikely to be sufficiently bright to contribute to the LyC leakage from Knot B. A generous upper limit to the LyC luminosity of the ULX can be estimated by extrapolating the X-ray power-law into the UV. Using the observed slope of $\Gamma = 1.7$ (Gross et al. 2021), we estimate the intrinsic 903 − 912 Å luminosity of the ULX to be $L_{912,ULX} \lesssim 6 \times 10^{39}$ erg s^{-1}. This is fainter than the observed LyC of Knot B, $L_{912,obs} = 2 \times 10^{40}$ erg s^{-1}, although it agrees within the observational uncertainty of $\pm 1.5 \times 10^{40}$ erg s^{-1}. Besides, more realistic ULX SED models predict even fainter LyC luminosities than we estimate, by 1-2 orders of magnitude (e.g., Fernández-Ontiveros et al. 2012; Gierliński et al. 2009). Regardless, the intrinsic stellar LyC emission we constrain from our population synthesis, $L_{912,int} = 6 \times 10^{41}$ erg s^{-1}, is two orders of magnitude higher than that estimated for the ULX. So, the stellar population alone can fully account for the observed LyC leakage from Knot B, with a relatively insignificant contribution from the ULX.

3.2. *Knot C*

Knot C is the region with the second-strongest LyC flux of Haro 11, with a detected LyC luminosity $L_{912,obs} = (0.9 \pm 0.7) \times 10^{40}$ erg s^{-1} (Table 2), or nominally about half of the Knot B luminosity. We note, however, that the large uncertainties on the LyC fluxes preclude a conclusive claim on the relative strengths of the emergent LyC from the knots. Knot C has been the prime candidate for LyC emission from Haro 11 based on its highest Lyα escape among the three knots, with $f_{esc,Ly\alpha} = 6$ % for Knot C, and $f_{esc,Ly\alpha} \lesssim 1\%$ for A and B (Östlin et al. 2021). Why does LyC appear fainter than that in Knot B, and what is the corresponding local escape fraction?

Our best stellar population fit to the combined COS G130M/1055 + G130M/1300 + G160M/1600 + MUSE spectrum of Knot C is shown in Figure 5, with detailed parameters in Table 3. It consists of two components: a population continuously formed for 15 Myr at SFR = 1.7 $M_\odot$ yr^{-1} and a single older population with age 100 Myr. The model fits the observed spectrum well (reduced $\chi^2 = 2.4$), with the P Cygni profiles of O VI, N V, C IV, and Si IV fit well, excluding ISM absorption, and clearly indicating the presence of $1-5$ Myr-old stars. As can be seen in Tables 2 and 3, our stellar population fit gives a total photoionization rate $Q_0 = 4 \times 10^{53}$ s^{-1}, which is within a factor of two of the value inferred from Hα. As Knot C appears to be a nuclear star cluster, a continuous star formation history is reasonable (Adamo et al. 2010).

The current episode of constant star formation is superimposed on an older, background population, which

is likely the diffuse, extended, bulge-like component. We allow the metallicities of the components to vary between observed values, $Z_{\rm obs} = 0.004$ from Menacho et al. (2021), and $Z = 0.001$. We note that the old component we find is a generic background population whose age is not well determined above ~ 30 Myr. Because its contribution to the spectrum is only in the optical continuum, it can be fitted with a wide range of age–extinction combinations. The high-resolution Starburst99 UV models are only available up to ages of 100 Myr. We have therefore also fit low-resolution Yggdrasil SSP models (Zackrisson et al. 2011) to the spectrum of Knot C and found a good fit with ages up to 2 Gyr and extinctions $E(B-V) < 0.8$, consistent with previously reported values (Sirressi et al. 2022). Our predicted FIR luminosity from dust processing is $L_{\rm FIR} = 2 \times 10^{43}$ erg s^{-1}.

Comparing our results to the S22 photometrically derived cluster parameters in Tables 3 and 4, we see that S22 find Knot C to be dominated by one massive cluster of age 15 Myr, which is likely the nuclear cluster. The cluster properties we obtain from the spectrum are consistent with S22 within the errors. Thus Knot C, undergoing continuous star formation for the last 15 Myr, has the oldest mass-weighted age in Haro 11, in contrast to the 2 Myr-dominated Knot B. While there are $1-5$ Myr stars present, their total mass in our model is $\sim 9 \times 10^6$ M$_\odot$, which is 3× lower than that in Knot B. Knot C therefore has a lower intrinsic ionizing luminosity than Knot B.

Our stellar population model gives a local escape fraction from Knot C of $f_{\rm esc,912}$= 0.051±0.043. Here, the uncertainty is dominated by observational error of 78%, while the model uncertainty is 30%. The escape fraction of Knot C may thus be higher than that of Knot B, 0.034 ± 0.029 (Table 3). So, despite appearing fainter in LyC than Knot B, Knot C may leak LyC more efficiently. The observed properties of Knot C are also consistent with it having the highest LyC escape among the knots. In addition to the highest Lyα escape fraction, Knot C exhibits the lowest neutral covering fraction $f_{\rm c,Si\ II} < 0.5$, corresponding to $f_{\rm c,HI} \sim 0.8$ (Chisholm et al. 2018) and the lowest neutral column density, as measured with the apparent optical depth method (Savage & Sembach 1991) applied to Si II, $\log(N_{\rm Si\ II}/{\rm cm}^{-2}) = 14.7$ (Table 2) (Östlin et al. 2021) .

On the other hand, its extinction is comparable to that of Knot B, suggesting a weak relation between dust extinction and LyC escape. Ionization-parameter mapping results are likewise ambiguous. On one hand, Knot C shows a strong [S II] $\lambda\lambda$6717,6731 deficiency of Δ[S II] $= -0.14$ (Östlin et al., in prep), suggestive of LyC escape (Wang et al. 2021; Pellegrini et al. 2012). On the other hand, the knot appears to be in a low ionization state, based on low $O_{32} \leq 3$ and [O III] λ5007/H$\alpha \leq 0.5$ and high [O II] λ3727/H$\alpha \sim 0.3$ (Keenan et al. 2017). As shown in Figure 5 of Keenan et al. (2017), it appears to have a high-ionization region extending to the east, but overall, Knot C appears to have low ionization relative to the rest of the galaxy. It moreover shows a confined morphology for the high-ionization region, with the O_{32} ratio transitioning smoothly and quickly to lower values into optically thick envelopes.

Despite some signatures of high optical depth, Knot C has the advantage of extensive stellar feedback. With a continuous star-formation history of 15 Myr (Table 3), Knot C has had a significant supernova history. S22 suggest that the mechanical feedback has been taking place even longer, over the last 40 Myr (Sirressi et al. 2022). The S22 feedback model can account for the energetics of the observed soft diffuse X-ray emission in Haro 11 reported by Grimes et al. (2007). We measure [S II]$\lambda\lambda$6716, 6731/H$\alpha = 0.26$ in our spectrum of Knot C, consistent with stellar photoionization. But Menacho et al. (2019) find that the combination of [O I]λ6300/Hα and [O III]λ5007/Hα ratios on the outskirts of Haro 11 indicates $200-600$ km/s shocks. They also find a ~ 2 kpc, high-ionization structure with Knot C at the center, that is likely a superbubble. Knot C also shows 1000 km s^{-1} gas (Menacho et al. 2019), which is difficult to explain with supernovae or stellar winds, and may instead be a signature of radiation-driven outflows (Komarova et al. 2021). Overall, the significant stellar feedback in Knot C, whether radiation- or mechanically dominated, may have cleared optically thin channels in its ISM, through which LyC photons can escape.

Similar to Knot B, Knot C contains a ULX that, based on its $0.3-8.0$ keV spectrum and luminosity, might be one of the most luminous soft ULXs known, with $L_{\rm X} = 4.5 \times 10^{40}$ erg s^{-1} (Prestwich et al. 2015; Gross et al. 2021). The X-ray emission likewise originates in two point sources, where the secondary object shows $L_{\rm X} \sim 2 \times 10^{40}$ erg s^{-1} (Gross et al. 2021). Prestwich et al. (2015) and Gross et al. (2021) explain its high luminosity by an IMBH of mass M$_\bullet >$ 20 M$_\odot$, undergoing super-Eddington accretion (Swartz et al. 2011; Kaaret et al. 2017), although it is also possible to be a neutron star binary, since compact object masses are poorly constrained. In turn, the blowout of inner-disk material in this intense accretion phase can result in a disk wind (e.g., Middleton et al. 2015). If the super-Eddington accretion drives an outflow with a mechanical luminosity similar to its X-ray luminosity (e.g., Justham & Schawinski 2012), the outflow power would be comparable

to the stellar wind power of Knot C, estimated to be 6×10^{40} erg s^{-1} (Sirressi et al. 2022). So, the ULX feedback may contribute significantly to gas clearing, promoting LyC escape.

To understand the role of the ULX in the LyC leakage from the knot, we estimate the ULX LyC output by extrapolating its X-ray power-law into the UV. For the observed spectral index $\Gamma = 2.1$, we estimate $L_{912,\rm ULX} \leq 2 \times 10^{40}$ erg s^{-1}. This is a generous upper limit, as Vinokurov et al. (2013) and Kaaret & Corbel (2009) show that more realistic model SEDs of supercritical accretion disks are even fainter in the UV. Our estimated ULX LyC luminosity is twice as bright as the observed LyC luminosity from Knot C, and thus the ULX can plausibly contribute LyC. However, our modelled stellar LyC of 2×10^{41} erg s^{-1} exceeds that of the ULX by at least an order of magnitude. Thus, if the ULX is responsible for some of the LyC emission from the region, its contribution may be unimportant compared to that of the stellar population. However, if its mechanical feedback dominates the gas clearing for the observed LyC, its LyC contribution may still be significant.

So, the stellar population of Knot C can alone account for the observed LyC leakage from this region. The soft, luminous ULX observed in this knot may be sufficiently bright to contribute to the LyC emission, but its intrinsic production is $< 10\%$ of the stellar emission. The ULX may be able to aid in the escape of Lyman radiation through mechanical feedback. Further investigation of the mechanical and radiative feedback of the ULXs is needed to conclusively establish their roles in the LyC leakage from Knot C.

3.3. *Knot A*

Knot A has also been predicted to be the LyC-leaking knot, based on ionization-parameter mapping, which Keenan et al. (2017) use to show that Knot A is responsible for a large, ∼kpc-sized region with high O_{32}. They find a central $O_{32} \sim 9$, consistent with the most extreme Green Peas, which are the largest class of local LyC leakers (e.g., Flury et al. 2022a). However, we do not detect LyC in Knot A. The 2σ upper limit of the LyC flux density from Knot A is $F_{912} < 3.3 \times 10^{-15}$ erg s^{-1}cm^{-2} Å^{-1} in the range $903-912$ Å, or $L_{912,\rm obs} < 2.8 \times 10^{40}$ erg s^{-1}.

To estimate the local escape fraction upper limit, we use our population synthesis results. Our stellar model for the spectrum of Knot A consists of three SSPs of ages 3 Myr, 4 Myr, and 13 Myr, as shown in Figure 3 and detailed in Table 3. The model fits the spectrum reasonably well (reduced $\chi^2 = 3.7$), accounting for both the continuum and age-sensitive features. The P Cygni profiles of O VI, N V, C IV, Si IV clearly indicate the presence of 3 Myr-old stars. Although the Wolf-Rayet He I λ1640 and 5608 Å and 4650 Å bumps are not included in Starburst99 models, these features are consistent with a ∼4 Myr population. With 1×10^7 M$_\odot$, this 4 Myr component dominates the stellar mass of Knot A, but is highly obscured, with $E(B-V) = 0.5$. It therefore has no FUV contribution, including in the age-sensitive P Cygni features, and the 3 Myr component can alone account for these profiles, while the dusty population contributes 25% of the optical luminosity. The 3 Myr and 4 Myr populations reproduce the observed photoionization rate from Hα within a factor of two (Tables 2 and 3). However, given that Knot A has the least dust among the knots, with previously reported extinction $E(B-V) \sim 0.2$ (Menacho et al. 2021), this discrepancy may indicate a modest mass overestimate in the 4-Myr component. Comparing with the S22 clusters in Table 4, our 4-Myr spectroscopic component is $10\times$ more massive than the 4-Myr S22 cluster, but has an $8\times$ higher extinction. Similar to the 14 Myr cluster found by S22, we find a 13 Myr component, with a matching mass but $2\times$ higher extinction. Lastly, the total FIR luminosity predicted by our model for the knot is 2.8×10^{43} erg s^{-1}.

The massive young populations we uncover in Knot A may possibly host VMS. This was previously suggested as an explanation for Knot A's broad blue bump (Keenan et al. 2017). Similar to Knot B, we evaluate the spectrum of Knot A for VMS signatures. We do not detect the blue-shifted O V λ1371 absorption common in VMS, and we measure the He II λ1640 EW = 2 Å, while VMS show > 3 Å (Martins et al. 2023). The observed red bump is broad and smooth, while the blue bump shows WR C IV λ4658. So, as in Knot B, we do not find evidence of VMS in Knot A. The above observations are instead consistent with classical WR stars.

From our modelled intrinsic LyC luminosity of the stellar populations, we estimate a 2σ upper limit to the escape fraction $f_{\rm esc,912} \leq 0.10$ (Table 3). Our non-detection thus does not conclusively rule out significant LyC escape in Knot A. Indeed, multiple lines of evidence point to some degree of LyC escape in Knot A. First, despite showing the lowest observed Lyα luminosity among the knots, $L_{\rm Ly\alpha} = 3 \times 10^{40}$ erg s^{-1}, the Lyα escape fraction of Knot A is $f_{\rm esc,Ly\alpha} = 1.2 \pm 0.12\%$ (Östlin et al. 2021), which is $2\times$ that of Knot B (Table 2). Nevertheless, this value is lower than that suggested by its reddening, implying that Lyα is strongly attenuated by dust scattering (Östlin et al. 2021). The neutral covering fraction is similar to that of Knot B, $f_c = 0.95 \pm 0.05$ (Östlin et al. 2021), and so is the column density, $\log(N_{\rm HI}/{\rm cm}^{-2}) = 20.7$ (Östlin et al. 2021).

Moreover, Knot A shows a number of signatures of low optical depth in ionization parameter mapping. Its [S II] deficiency is most extreme among the knots, Δ[S II] = −0.19 (Östlin et al., in prep), predicting the highest $f_{\rm esc,LyC}$ (Wang et al. 2021). Most importantly, Keenan et al. (2017) report high-O_{32} gas originating at Knot A and spreading to distances of > 2 kpc, and Menacho et al. (2019) observe it to > 4 kpc as high [O III]/Hα, signaling a transparent medium in the transverse directions. In fact, the O_{32} ratio does not transition smoothly into lower values at the edges of this region, strongly implying low optical depth in the plane of the sky. Menacho et al. (2019) show that this structure exhibits the highest ionization, [O III]/H$\alpha \gtrsim 3$, in velocity bins from −300 km s^{-1} to −150 km s^{-1}, while the central [O III]/H$\alpha \sim 1$. This suggests that the high-ionization structure is likely an optically thin outflow driven by LyC from the knot, but its axis is not coincident with our line of sight.

The main implication of our results in light of IPM observations is therefore that LyC escape must be highly anisotropic. While we do not detect LyC in Knot A, it is likely that the leakage, if any, occurs through a channel not coincident with our line of sight (e.g., Zastrow et al. 2011). This is consistent with the Lyα peak velocity separation, which is highest in Knot A, $v_{\rm sep,Ly\alpha} \sim 500$ km s^{-1}, compared to the other two knots. Such large $v_{\rm sep,Ly\alpha}$ is consistent with escape fractions < 1% (Flury et al. 2022b).

4. DISCUSSION

We find that the LyC-emitting regions in Haro 11 are Knots B ($L_{912,\rm obs} = 2.3 \pm 1.8 \times 10^{40}$ erg s^{-1}) and C ($L_{912,\rm obs} = 0.9 \pm 0.7 \times 10^{40}$ erg s^{-1}). We determine their respective LyC escape fractions to be $f_{\rm esc,912}$= 3.4 ± 2.9% and 5.1 ± 4.3% (Table 3). The total LyC-luminosity-weighted escape fraction of Haro 11 is $f_{\rm esc,912} = 3.9 \pm 3.4$%, consistent with 3.3 ± 0.7% obtained by Leitet et al. (2011). Knot B appears to dominate in LyC luminosity, with the caveat that the low signal-to-noise in our LyC observations prevents a conclusive determination of which knot dominates. At face value, Knot B is responsible for 2/3 of the total observed flux, and it has ∼ 3× higher mass in 1 – 5 Myr-old stars than Knot C (Table 3), which is the age of peak LyC production. Thus Knot B strongly dominates the ionizing photon production. However, it has almost full neutral covering (Östlin et al. 2021) and high extinction (Table 3). In comparison, Knot C is a more evolved region of constant star formation for the last 15 Myr, with a commensurate history of supernova feedback, possible LLAGN feedback, and low neutral covering fraction (Sirressi et al. 2022; Östlin et al. 2021). Our findings highlight the sensitivity of LyC escape to the star-formation rate, age, and optical depth.

Thus, Knot B both has more young stars and emits more strongly in LyC, but has a slightly lower escape fraction than Knot C. Our results underscore the fact that *LyC escape fraction and escaping LyC luminosity are separate quantities.* In Haro 11, Knot B seems to produce the greatest LyC emission because it strongly dominates in LyC production. But its large gas and dust content apparently keeps its local escape fraction lower than the more evolved, and cleared, Knot C. On the other hand, Knot A shows similar age and extinction to Knot B, but we do not detect it in LyC. It is thus the interplay of star formation intensity, age, gas clearing, and/or line-of-sight orientation that determines the efficiency and detection of LyC escape. Tracers of $f_{\rm esc,912}$ alone are insufficient indicators of escaping LyC luminosity along the line of sight.

Flury et al. (2022b) connect LyC properties to star formation density, Lyα properties, and O_{32} in 66 local star-forming galaxies, including Green Peas. They find possible evidence for two modes of LyC escape in the most extreme starbursts, dictated by whether stellar feedback is wind-dominated or radiation-dominated. One population shows younger ages, higher O_{32}, and low metallicity, suggesting strong radiation-dominated feedback, which may be linked to optically thin, radiation-driven winds (Komarova et al. 2021). On the other hand, the somewhat older starbursts with lower O_{32} and higher metallicity likely leak LyC with the help of superwinds (e.g., Heckman et al. 2011; Zastrow et al. 2013), and these show lower $f_{\rm esc,LyC}$. If Knot A is indeed an anisotropic LyC emitter as evidenced by ionization-parameter mapping (Keenan et al. 2017), then it falls into the radiation-dominated category, consistent with its very high ionization parameter, and other radiation-dominated features (Section 3.3; Keenan et al. 2017). Knot B may likewise be radiation-dominated based on its high O_{32} and young age, with the caveat that its metallicity is close to solar. Finally, Knot C has low O_{32} and is apparently dominated by mechanical feedback, given its extensive supernova history (Sirressi et al. 2022). Since we observe multiple stellar generations in each region, it is likely that both modes are at play, with their relative importance to be established.

Haro 11 is a local Green Pea analog, showing O_{32} and other radiation-dominated properties characteristic of these objects (Micheva et al. 2017; Keenan et al. 2017). These properties are linked to Knot A, which turns out to not show direct detection in LyC, although IPM strongly implies that the region is optically thin in

other sightlines. This additionally stresses the dependence of the escape fraction on the geometrical distribution of dust and neutral gas along the line of sight. The fact that the detected LyC from Haro 11 originates from regions other than Knot A further demonstrates that LyC emission from Green Peas may be more complex than consideration of a single starburst (e.g., Micheva et al. 2018). Notably, the global O_{32} for Haro 11 is only 2.5 (James et al. 2013), which is on the low side for a GP. This O_{32} is consistent with that of unresolved GPs in the Low-redshift Lyman Continuum Survey (LzLCS), containing the largest sample of local LCEs to date. The LzLCS GPs show $f_{\rm esc,LyC} = 1 - 4\%$ for similar O_{32}. In addition, the ionizing photon production efficiencies we estimate are $\log(\xi_{\rm ion}) = 25.32$ for Knot B and 25.22 for Knots A and C. These values are lower than that of reionization-era galaxies, $25.4 - 25.8$ (Simmonds et al. 2023; Saxena et al. 2023; Atek et al. 2024), or local strong LyC leakers, $25.6 - 26$ (Schaerer et al. 2016). But they are consistent with the standard values assumed in reionization models (Robertson et al. 2015).

Our spatially resolved study thus uncovers how some of the global properties we observe at higher redshifts may arise from multiple star-forming regions of widely differing properties. In particular, the regions dominating the ionization may not be the primary LyC sources in our line of sight, and more evolved regions' contribution should not be discounted.

4.1. *Implications for Lyα as a Diagnostic of LyC*

As LyC emission is difficult to observe directly, indirect tracers are required to identify LyC leakers. Lyα is expected to correlate with LyC escape, as it is also sensitive to the hydrogen column density. Radiative transfer simulations (e.g., Verhamme et al. 2015) and observations of several LCEs (Verhamme et al. 2017) confirm a tight relationship between Lyα and LyC escape. The LzLCS survey shows that Lyα width and peak separation are some of the strongest indirect predictors of LyC escape fractions (Flury et al. 2022b). With their new, larger sample, the authors reproduce the anti-correlation between Lyα peak velocity separation $v_{\rm sep,Ly\alpha}$ and LyC escape fraction, $f_{\rm esc,LyC}$, first established by Izotov et al. (2018).

Our findings in Haro 11 are consistent with these Lyα predictions. As shown in Table 2, the Lyα peak separations observed in Knots A, B, and C are 530, 409, and 400 km s^{-1}, respectively (Östlin et al. 2021), decreasing with increasing $f_{\rm esc,LyC}$. Knots B and C are consistent with the Flury et al. (2022b) $v_{\rm sep,Ly\alpha} - f_{\rm esc,LyC}$ relation, which predicts $f_{\rm esc,LyC} \sim 0.03$ for $v_{\rm sep,Ly\alpha} =$ 400 km s^{-1}. The two LCE knots are also consistent with a $f_{\rm esc,Ly\alpha} - f_{\rm esc,LyC}$ correlation, where Knot C has a higher $f_{\rm esc,Ly\alpha}$ and a slightly higher $f_{\rm esc,912}$. We calculate the luminosity-weighted average Lyα escape fraction for the three knots to be $f_{\rm esc,Ly\alpha} = 4.2 \pm 0.6\%$. We also estimate the global Lyα peak velocity separation by combining the Lyα profiles of the three knots, obtaining $v_{\rm sep,Ly\alpha} = 410 \pm 70$ km s^{-1}. Our luminosity-weighted LyC escape fraction $f_{\rm esc,912} = 3.9 \pm 3.4\%$ is consistent with the averaged $v_{\rm sep,Ly\alpha}$ according to the Flury et al. (2022b) relation. These values account only for Lyα emission from the knots, and not diffuse Lyα observed outside of them (Östlin et al. 2009).

The efficiency of Lyα escape, or its escape fraction, can provide insight into LyC radiative transfer. Knot C has both the highest Lyα luminosity and $f_{\rm esc,Ly\alpha}$ among the knots, and its $f_{\rm esc,912}$ is indeed likely the highest despite the LyC luminosity being only half of that in Knot B. So, *while the LyC and Lyα escape fractions correlate, the emerging LyC and Lyα luminosities do not necessarily do so.*

As for the shape of the Lyα profiles, Knot A and B clearly show broader Lyα red peaks than Knot C, with their respective widths 302 km s^{-1}, 338 km s^{-1}, and 195 km s^{-1}, suggesting higher optical depth and low LyC escape (Östlin et al. 2021). The Lyα red peak width specifically points to Knot B as the weakest leaker, inconsistent with our results. Since both Knots A and B show neutral covering fractions close to unity (Table 2; Östlin et al. 2021), it appears that the correlation of Lyα red peak width with $f_{\rm esc,LyC}$ is not as strong when considering individual star-forming regions instead of integrated galaxy properties. The Lyα profile of Knot C, on the other hand, is narrow, but with a higher red peak asymmetry than in Knots A and B (Rivera-Thorsen et al. 2017; Östlin et al. 2021). Kakiichi & Gronke (2021) show that higher red peak asymmetry around its center points to LyC escape through a hole-ridden ISM, or a picket fence structure, as the asymmetry is seen to correlate with ISM porosity in their radiation-hydrodynamic simulations. This arises because the asymmetry of the red peak traces the presence of both optically thin and thick channels, while a symmetric red peak indicates isotropic leakage.

One inconsistency we see in Lyα predictions is in the non-detected Knot A, where its peak velocity separation is highest among the knots, but its Lyα escape fraction is twice that of Knot B. The peak velocity separation thus implies the lowest LyC $f_{\rm esc,LyC}$ among the knots, while the Lyα escape fraction suggests it should be higher than that in Knot B. A likely explanation for this may be that the LyC is emerging in directions transverse to our line of sight, as implied by ionization-

parameter mapping (Section 3.3), while Lyα can be enhanced by scattering into our line of sight. The observed Lyα luminosity of Knot A is notably the lowest among the knots, and the intrinsic LyC we estimate is 3× lower than that of Knot B (Table 3), while exhibiting a similar covering fraction, column density, and thus similarly broad red Lyα peak. Lastly, it is important to note that the Lyα relations described above were established for unresolved galaxies, which likely also consist of multiple star-forming regions with varying properties. In our spatially resolved study, we connect Lyα profiles from smaller, ∼1-kpc apertures to individual knot properties, providing a view of separate components that may make up the integrated Lyα observations.

Although most of our results agree well with Lyα predictions, there are still significant differences in the escape conditions for LyC vs. Lyα. The maximum column density at which Lyα can escape is $\log(N_{\rm HI}/{\rm cm}^{-2}) < 13$, while the threshold for LyC is $\log(N_{\rm HI}/{\rm cm}^{-2}) < 17$. So, the four orders of magnitude of difference provide a parameter space where gas can be optically thin in LyC but not in Lyα. Another major difference in the escape mechanisms is scattering: Lyα scatters strongly, modulating its escape path and additionally promoting dust absorption relative to LyC. Dijkstra et al. (2016) simulate the radiative transfer of Lyman radiation in multiphase ISM to investigate the relationship between LyC and Lyα escape fractions. They find a positive correlation, as expected, but with significant scatter at higher Lyα escape fractions that is driven by gas covering fraction. The corresponding LyC escape fractions in this region are lower than expected from the correlation, decreasing with higher covering fractions. The scatter extends at least two orders of magnitude, consistent with observations (Flury et al. 2022b), showing that the ISM porosity introduces appreciable stochasticity to the relationship between LyC and Lyα radiation. This can also provide a context for the Lyα vs LyC observations of Knot A.

Thus, Lyα properties can provide clues to LyC escape conditions, though not without additional independent tracers. Our Haro 11 study shows that Lyα peak velocity separation is consistent with it tracing $f_{\rm esc,LyC}$, where the knots fall on the observed relation within scatter. But the Lyα luminosity, red peak width, and escape fraction do not correlate directly with LyC escape in regions of varying gas optical depth and covering. Our results underscore the significant distinctions in Lyα and LyC radiative transfer, and that further study into the effects of ISM morphology and anisotropy of LyC escape is needed.

4.2. *IPM and Anisotropy of LyC Escape*

Ionization-parameter mapping relies on nebular emission line ratios with different ionization potentials to find regions of low optical depth, where high-ionization species dominate. This serves as an indirect tracer for LyC escape (Pellegrini et al. 2012).

Our resolved observations of the LyC-emitting regions of Haro 11 are not fully consistent with predictions from IPM, if isotropic escape is assumed. Most importantly, in Knot A, IPM demonstrates LyC escape conditions transverse to the line of sight (Keenan et al. 2017, ; Section 3.3). Yet we find no LyC detection in the COS aperture, which probes the line of sight. As noted above, this suggests that LyC escape may be extremely anisotropic. This is also implied from our observations of Knot B, which leaks LyC despite being almost fully covered in neutral gas, implying a narrow escape path. Knot C, on the other hand, is seen to be in a low-ionization state, implying high optical depth in LyC. Yet we find it to have the highest LyC escape fraction. Thus the IPM predictions appear to be sensitive to line-of-sight effects.

Hydrodynamic simulations of starbursts at $z = 4 - 6$ by Cen & Kimm (2015) confirm that the LyC escape fraction depends strongly on the viewing angle. They find that only highly ionized, evacuated channels with small solid angles allow significant LyC propagation. Indeed, the observed scatter in LyC escape fractions with respect to correlated starburst properties at $z \sim 3$ and $z < 0.4$ points to a line of sight effect, where partial ISM clearing results in limited transparent paths (Flury et al. 2022b; Nestor et al. 2011). Several nearby starbursts with active stellar feedback likewise exhibit narrow ionization cones (Zastrow et al. 2011, 2013). The line-of-sight bias is thus crucial to account for in reionization studies at all redshifts. Anisotropy of LyC escape, dictated by the gas-clearing mechanisms such as winds and supernovae, as well as the optical depth and ionization structure, need to be accounted for when using IPM as a predictor for LyC escape. This may be even more important if accretion-driven feedback is responsible for the necessary gas clearing.

Thus, our observations of Haro 11 offer important data on what information IPM does and does not provide on LyC escape. While it gives insight into the ionization structure in the plane of the sky, additional tracers probing line-of-sight conditions are required to identify objects in which LyC can be directly detected.

4.3. *X-ray Sources and LyC Escape*

The two LyC-leaking Knots B and C both host ULXs, while the undetected Knot A is purely star-forming. This interesting coincidence raises the question of the

role of accretors in LyC escape, which has been a major problem in cosmic reionization (e.g, Volonteri & Gnedin 2009; Madau & Haardt 2015). Although the ULX LyC contribution is likely negligible in Knot B, the ULX in Knot C, which may be an LLAGN, may contribute to the LyC leakage from the region at the $\lesssim 10\%$ level. On the other hand, the focused mechanical feedback that can be expected from these X-ray sources might contribute to clearing optically thin channels for LyC escape in both Knots B and C. Low-accretion, hard X-ray sources as that seen in Knot B may produce jets of substantial mechanical power (e.g., Merloni & Heinz 2013; May et al. 2018). Likewise, the soft, super-Eddington sources, such as the one hosted by Knot C, can also drive radiation-driven disk winds that may be important (e.g., Middleton et al. 2015). These feedback mechanisms may significantly enhance ULX contributions to LyC escape.

The question of the role of accretors in cosmic reionization is all the more important in light of the observed excess X-ray emission in early-universe galaxy analogs. For instance, Kaaret et al. (2011) observe an increased X-ray luminosity per star formation rate $L_{\rm X}$/SFR in blue compact dwarfs (BCDs), and Brorby et al. (2014) find the BCD X-ray luminosity function to have 10× the normalization observed in solar-metallicity galaxies. Also, Douna et al. (2015) find 10× more high-mass X-ray binaries (HMXBs) per SFR bin in $< 0.2\ Z_\odot$ galaxies than in solar-metallicity objects. Extremely metal poor galaxies (XMPG, $Z < 0.05\ Z_\odot$) show more ULXs than higher-metallicity galaxies (Prestwich et al. 2013). Moreover, Basu-Zych et al. (2013) find that a sample of $z < 0.1$ Lyman break analogs (LBAs), including Haro 11, likewise exhibit a higher $L_{\rm X}$/SFR than solar-metallicity galaxies. Their interpretation is that lower metallicity results in more luminous HMXBs, as weaker stellar winds lead to more massive compact objects. Brorby et al. (2016) quantify this $L_{\rm X} - {\rm SFR} - {\rm Z}$ relation, where $L_{\rm X}$/SFR increases with lower log(O/H). Finally, Dittenber et al. (2020) find that the majority of local Lyα emitters, and thus candidates for LyC escape, may be driven by ULXs, finding a connection between Lyα escape and HMXBs and/or LLAGN. Thus, metal-poor starbursts in the early universe likely formed an overabundance of X-ray binaries, which may have contributed to the process of reionization.

From our LyC study of Haro 11, we see that LyC-emitting regions may coincide with ULX sites, but the role, if any, of accretors in ionizing radiation production and mechanical feedback remains to be clarified.

5. SUMMARY AND CONCLUSIONS

Haro 11 is a key object to understanding cosmic reionization as it is the closest, and first, confirmed local LyC emitter. It is dominated by three star-forming Knots A, B, and C of widely varying properties, and since the original, spatially unresolved detection, it has remained unclear which of these three regions is responsible for the observed LyC emission. We therefore obtained new HST/COS G130M/1055 observations of each of the knots in the range $900-1200$ Å, which reveal that Knots B and C are the LyC emitters toward our line of sight. Their respective $903-912$ Å luminosities are $1.9\pm1.5\times10^{40}$ erg s^{-1} and $0.9\pm0.7\times10^{40}$ erg s^{-1}. So, Knot B seems to dominate the leaking LyC luminosity of Haro 11, accounting for $66\pm50\%$ of the detected flux in $903-912$ Å, and Knot C accounts for $35\pm25\%$. The total Haro 11 LyC luminosity is $2.9\pm1.0\times10^{40}$ erg s^{-1}.

We perform stellar population synthesis to constrain the stellar parameters and thus local LyC escape fractions of each knot. For this, we combine our new COS G130M/1055 with Sirressi et al. (2022) COS G130M/1300 + G160M/1600, as well as Menacho et al. (2019) MUSE spectra. Fitting Starburst99 models to each knot's spectrum, we find that Knot B, the brightest LyC emitter, is dominated by a $\sim$ 1 Myr, 2×10^7 M$_\odot$ heavily obscured component. Knot C is best fit with a continuous star formation history for $\sim$ 15 Myr with stellar mass of 3×10^7 M$_\odot$ and low obscuration. Knot A is dominated by a $\sim$ 4 Myr, 1×10^7 M$_\odot$ highly obscured population. Our modeling thus uncovers massive, young, obscured stellar populations in Knot B and Knot A, which dominate the ionizing photon production in their respective regions but have minimal FUV imprint and contribute $< 40\%$ in the optical. We do not see conclusive evidence of Very Massive Stars in any of the knots. Instead, we find clear signatures of classical WR stars in Knots A and B.

The primary tracer of the young populations is the large Hα luminosity, which we reproduce with our models within a factor of two or better. Moreover, Haro 11 shows a large FIR luminosity, $L_{\rm FIR} = 2.7\times10^{44}$ erg s^{-1}, that qualifies it as a LIRG. Our dusty stellar population models for the three knots combined account for 1.7×10^{44} erg s^{-1}, which is within 60% of the observed integrated FIR radiation. Thus the model estimates and observed values are in reasonable agreement, especially considering that the IRAS aperture includes the entire galaxy. Sirressi et al. (2022) photometrically detect $7-11$ clusters in each knot, with ages $1-15$ Myr and masses up to 5×10^7 M$_\odot$ (Table 3). Our 3-component spectroscopic models capture the aggregate young, UV-dominant populations, as well as the $\sim$ 15 Myr generation that does not contribute significant LyC. The spec-

trum of Knot C additionally shows an old background population with an age up to ~ 2 Gyr.

The corresponding LyC escape fractions in the range $903 - 912$ Å are $f_{\rm esc,912} = 3.4 \pm 2.9\%$ for Knot B and $5.1 \pm 4.3\%$ for Knot C. In the case of Knot A, we place a 2σ upper limit to the escape fraction of $f_{\rm esc,912} \leq 10\%$. The luminosity-weighted escape fraction for the entirety of Haro 11 is $f_{\rm esc,912} = 3.9 \pm 3.4\%$, consistent with Leitet et al. (2011).

Our results underscore that the LyC escape fraction ($f_{\rm esc,912}$) and escaping LyC luminosity ($L_{912,\rm obs}$) are distinct fundamental parameters for characterizing LyC escape. Although we find that the majority of Haro 11's LyC flux likely originates from Knot B, the values above demonstrate that its local escape fraction appears to be lower than that of the LyC-fainter Knot C. The reason is that Knot B has by far the highest ionizing photon production; but it exhibits the largest amount of neutral gas among the knots, and in particular, it has a covering fraction close to unity (Gao et al. 2022; Östlin et al. 2021). This results in a potentially lower escape fraction. On the other hand, Knot C is intrinsically fainter in LyC due to an older mass-weighted age, but it is significantly less obscured. Some of its gas has likely been evacuated by feedback, as its HI covering fraction is $f_{\rm c,HI} \sim 0.8$ and its neutral column density is the lowest among the knots (Table 2; Östlin et al. 2021). Characterizing LyC emission by only $f_{\rm esc,912}$ would prioritize Knot C over B, whereas Knot B is in fact the more luminous LyC emitter. Thus, although the escape fraction is often emphasized in the literature, the relevant parameter is the convolution of the escape fraction and the intrinsic LyC luminosity, since both drive the observable LyC luminosity and the number of ionizing photons leaked into the IGM.

We also use our new observations to test Lyα as a LyC escape tracer by comparing our results to Lyα-based predictions. We see a correlation of $f_{\rm esc,912}$ with the observed Lyα luminosity, and an inverse relation with Lyα peak velocity separation $v_{\rm sep,Ly\alpha}$, as expected. But the Lyα escape fraction $f_{\rm esc,Ly\alpha}$ does not consistently trace LyC escape. While Knot C has both the highest Lyα and LyC escape fractions, the lowest $f_{\rm esc,Ly\alpha}$ in Knot B incorrectly predicts it to be the weakest LyC leaker. The Lyα red peak width similarly points to Knot C as the strongest leaker and Knot B as the weakest, with the latter not consistent with our observations. So, the observed Lyα luminosity and peak velocity separation appear to more consistently correlate with LyC escape, while $f_{\rm esc,Ly\alpha}$ and Lyα red peak width are less consistent tracers. However, we stress that these results are based on only three star-forming knots in this galaxy.

There are important implications from the fact that Knot A is not detected in the LyC, despite it driving the Green Pea properties of Haro 11. Green Peas are the largest class of local LyC emitters, and their radiation properties strongly correlate with $f_{\rm esc,LyC}$ (Flury et al. 2022a,b). Knot A has therefore been predicted to be a leaking knot based on its ionization parameter, which is the highest of the three knots (Keenan et al. 2017). First, its non-detection highlights the potential importance of multiple star-forming regions driving the LyC escape in Green Peas. In Haro 11, we see that while the knot dominating the GP properties is not directly detected, other knots are LyC emitters. Many GPs, like Haro 11, are mergers hosting multiple star-forming knots. So, while GP properties and signatures of radiation-dominated feedback are alone insufficient to predict LyC emission , the multiplicity of starbursts may be important. Micheva et al. (2018) noted the potential role of two-stage starbursts in LyC emitters. On the other hand, Knot A shows clear signatures of density-bounded conditions in the plane of the sky (Keenan et al. 2017). It is therefore likely that Knot A is leaking LyC transverse to our line of sight, as seen in, e.g., NGC 5253 (Zastrow et al. 2011). This implies that LyC escape must be highly anisotropic, as predicted by simulations (Cen & Kimm 2015) and inferred from observations (Nestor et al. 2011; Flury et al. 2022b).

Lastly, we note the intriguing coincidence that the two LyC-leaking knots are the hosts of the only two ULXs in Haro 11 (Prestwich et al. 2015; Gross et al. 2021). Neither of the ULXs appear to contribute significantly to the LyC emission, especially considering that the stellar populations dominate the UV light by $1 - 2$ orders of magnitude. Nevertheless, the X-ray sources may promote LyC escape through accretion-dominated mechanical feedback, where powerful disk winds and jets may clear optically thin channels. A multitude of studies show that reionization-era analogs, such as LBAs and BCDs, have an overabundance of ULXs (e.g., Dittenber et al. 2020; Brorby et al. 2014; Basu-Zych et al. 2013; Kaaret et al. 2011). Further investigation is thus required into both the ultraviolet emission and mechanical feedback of ULXs, in order to determine their role in LyC escape.

We thank Paul Draghis and Daniel Schaerer for useful discussions. This work was supported by NASA grant to M.S.O HST-GO-16260. A. Adamo acknowledges the support of the Swedish Research Council, Vetenskapsrådet grant 2021-05559. JMMH is funded by Spanish MCIN/AEI/10.13039/501100011033 grant PID2019-107061GB-C61. D.K. is supported by the Centre National d'Études Spatiales (CNES)/Centre National de la Recherche Scientifique (CNRS); convention no 230400. The Cosmic Dawn Center (DAWN) is funded by the Danish National Research Foundation under grant DNRF140. Lastly, we thank the anonymous referee for helpful suggestions that improved the manuscript.

This research is based on observations made with the NASA/ESA Hubble Space Telescope obtained from the Space Telescope Science Institute, which is operated by the Association of Universities for Research in Astronomy, Inc., under NASA contract NAS 5–26555. These observations are associated with programs 16260, 15352, and 13017. This research is also based on observations collected at the European Southern Observatory under ESO programme 096.B-0923(A). .

The *HST* data used in this paper can be found in MAST: 10.17909/p40f-yy93

Facilities: HST(COS), VLT(MUSE)

Software: Starburst99 (Leitherer et al. 1999, 2014), Astropy (Astropy Collaboration et al. 2022), LMFIT (Newville et al. 2016), Matplotlib (Hunter 2007)

REFERENCES

Adamo, A., Östlin, G., Zackrisson, E., et al. 2010, MNRAS, 407, 870, doi: 10.1111/j.1365-2966.2010.16983.x

Astropy Collaboration, Price-Whelan, A. M., Lim, P. L., et al. 2022, apj, 935, 167, doi: 10.3847/1538-4357/ac7c74

Atek, H., Labbé, I., Furtak, L. J., et al. 2024, Nature, 626, 975, doi: 10.1038/s41586-024-07043-6

Basu-Zych, A. R., Lehmer, B. D., Hornschemeier, A. E., et al. 2013, ApJ, 774, 152, doi: 10.1088/0004-637X/774/2/152

Bergvall, N., Zackrisson, E., Andersson, B. G., et al. 2006, A&A, 448, 513, doi: 10.1051/0004-6361:20053788

Bouwens, R. J., Illingworth, G. D., Oesch, P. A., et al. 2012, ApJL, 752, L5, doi: 10.1088/2041-8205/752/1/L5

Brorby, M., Kaaret, P., & Prestwich, A. 2014, MNRAS, 441, 2346, doi: 10.1093/mnras/stu736

Brorby, M., Kaaret, P., Prestwich, A., & Mirabel, I. F. 2016, MNRAS, 457, 4081, doi: 10.1093/mnras/stw284

Calzetti, D., Armus, L., Bohlin, R. C., et al. 2000, ApJ, 533, 682, doi: 10.1086/308692

Cen, R., & Kimm, T. 2015, ApJL, 801, L25, doi: 10.1088/2041-8205/801/2/L25

Chisholm, J., Gazagnes, S., Schaerer, D., et al. 2018, A&A, 616, A30, doi: 10.1051/0004-6361/201832758

Clarke, C., & Oey, M. S. 2002, MNRAS, 337, 1299, doi: 10.1046/j.1365-8711.2002.05976.x

Cullen, F., McLure, R. J., McLeod, D. J., et al. 2023a, MNRAS, 520, 14, doi: 10.1093/mnras/stad073

Cullen, F., McLeod, D. J., McLure, R. J., et al. 2023b, arXiv e-prints, arXiv:2311.06209, doi: 10.48550/arXiv.2311.06209

Danforth, C. W., Keeney, B. A., Stocke, J. T., Shull, J. M., & Yao, Y. 2010, ApJ, 720, 976, doi: 10.1088/0004-637X/720/1/976

Danforth, C. W., Keeney, B. A., Tilton, E. M., et al. 2016, ApJ, 817, 111, doi: 10.3847/0004-637X/817/2/111

Dashtamirova, D., White, J., & Sahnow, D. 2019, Changes in the COS/FUV Dark Rate: Impact on the Monitoring Program and Background Extraction Regions, Instrument Science Report COS 2019-11, 17 pages

Dijkstra, M., Gronke, M., & Venkatesan, A. 2016, ApJ, 828, 71, doi: 10.3847/0004-637X/828/2/71

Dittenber, B., Oey, M. S., Hodges-Kluck, E., et al. 2020, ApJL, 890, L12, doi: 10.3847/2041-8213/ab723e

Douna, V. M., Pellizza, L. J., Mirabel, I. F., & Pedrosa, S. E. 2015, A&A, 579, A44, doi: 10.1051/0004-6361/201525617

Ekström, S., Georgy, C., Eggenberger, P., et al. 2012a, A&A, 537, A146, doi: 10.1051/0004-6361/201117751
—. 2012b, A&A, 537, A146, doi: 10.1051/0004-6361/201117751
Faucher-Giguère, C.-A. 2020, MNRAS, 493, 1614, doi: 10.1093/mnras/staa302
Fernández-Ontiveros, J. A., Prieto, M. A., Acosta-Pulido, J. A., & Montes, M. 2012, in Journal of Physics Conference Series, Vol. 372, Journal of Physics Conference Series, 012006, doi: 10.1088/1742-6596/372/1/012006
Flury, S. R., Jaskot, A. E., Ferguson, H. C., et al. 2022a, ApJS, 260, 1, doi: 10.3847/1538-4365/ac5331
—. 2022b, ApJ, 930, 126, doi: 10.3847/1538-4357/ac61e4
Fontanot, F., Cristiani, S., Pfrommer, C., Cupani, G., & Vanzella, E. 2014, MNRAS, 438, 2097, doi: 10.1093/mnras/stt2332
Fontanot, F., Cristiani, S., & Vanzella, E. 2012, MNRAS, 425, 1413, doi: 10.1111/j.1365-2966.2012.21594.x
Fujita, A., Martin, C. L., Mac Low, M.-M., & Abel, T. 2003, ApJ, 599, 50, doi: 10.1086/379276
Gao, Y., Gu, Q., Shi, Y., et al. 2022, A&A, 661, A136, doi: 10.1051/0004-6361/202142309
Georgy, C., Ekström, S., Eggenberger, P., et al. 2013, A&A, 558, A103, doi: 10.1051/0004-6361/201322178
Giallongo, E., Grazian, A., Fiore, F., et al. 2015, A&A, 578, A83, doi: 10.1051/0004-6361/201425334
Gierliński, M., Done, C., & Page, K. 2009, MNRAS, 392, 1106, doi: 10.1111/j.1365-2966.2008.14166.x
Grimes, J. P., Heckman, T., Strickland, D., et al. 2007, ApJ, 668, 891, doi: 10.1086/521353
Gross, A. C., Prestwich, A., & Kaaret, P. 2021, MNRAS, 505, 610, doi: 10.1093/mnras/stab1331
Guseva, N. G., Izotov, Y. I., Fricke, K. J., & Henkel, C. 2012, A&A, 541, A115, doi: 10.1051/0004-6361/201118742
Hassan, S., Davé, R., Mitra, S., et al. 2018, MNRAS, 473, 227, doi: 10.1093/mnras/stx2194
Heckman, T. M., Borthakur, S., Overzier, R., et al. 2011, ApJ, 730, 5, doi: 10.1088/0004-637X/730/1/5
Helou, G., Khan, I. R., Malek, L., & Boehmer, L. 1988, ApJS, 68, 151, doi: 10.1086/191285
Hunter, J. D. 2007, Computing in Science & Engineering, 9, 90, doi: 10.1109/MCSE.2007.55
Izotov, Y. I., Orlitová, I., Schaerer, D., et al. 2016a, Nature, 529, 178, doi: 10.1038/nature16456
Izotov, Y. I., Schaerer, D., Thuan, T. X., et al. 2016b, MNRAS, 461, 3683, doi: 10.1093/mnras/stw1205
Izotov, Y. I., Worseck, G., Schaerer, D., et al. 2018, MNRAS, 478, 4851, doi: 10.1093/mnras/sty1378
James, B. L., Tsamis, Y. G., Walsh, J. R., Barlow, M. J., & Westmoquette, M. S. 2013, MNRAS, 430, 2097, doi: 10.1093/mnras/stt034
James, B. L., Berg, D. A., King, T., et al. 2022, arXiv e-prints, arXiv:2206.01224. https://arxiv.org/abs/2206.01224
Jaskot, A. E., Oey, M. S., Scarlata, C., & Dowd, T. 2017, ApJL, 851, L9, doi: 10.3847/2041-8213/aa9d83
Justham, S., & Schawinski, K. 2012, MNRAS, 423, 1641, doi: 10.1111/j.1365-2966.2012.20985.x
Kaaret, P., & Corbel, S. 2009, ApJ, 697, 950, doi: 10.1088/0004-637X/697/1/950
Kaaret, P., Feng, H., & Roberts, T. P. 2017, Annual Review of Astronomy and Astrophysics, 55, 303, doi: 10.1146/annurev-astro-091916-055259
Kaaret, P., Schmitt, J., & Gorski, M. 2011, ApJ, 741, 10, doi: 10.1088/0004-637X/741/1/10
Kakiichi, K., & Gronke, M. 2021, ApJ, 908, 30, doi: 10.3847/1538-4357/abc2d9
Keenan, R. P., Oey, M. S., Jaskot, A. E., & James, B. L. 2017, ApJ, 848, 12, doi: 10.3847/1538-4357/aa8b77
Komarova, L., Oey, M. S., Krumholz, M. R., et al. 2021, ApJL, 920, L46, doi: 10.3847/2041-8213/ac2c09
Kunth, D., Leitherer, C., Mas-Hesse, J. M., Östlin, G., & Petrosian, A. 2003, ApJ, 597, 263, doi: 10.1086/378396
Kunth, D., & Sargent, W. L. W. 1981, A&A, 101, L5
Leitet, E., Bergvall, N., Piskunov, N., & Andersson, B.-G. 2011, Astronomy & Astrophysics, 532, A107, doi: 10.1051/0004-6361/201015654
Leitherer, C., Ekström, S., Meynet, G., et al. 2014, ApJS, 212, 14, doi: 10.1088/0067-0049/212/1/14
Leitherer, C., Schaerer, D., Goldader, J. D., et al. 1999, ApJS, 123, 3, doi: 10.1086/313233
Ma, X., Hopkins, P. F., Kasen, D., et al. 2016, MNRAS, 459, 3614, doi: 10.1093/mnras/stw941
Madau, P., & Fragos, T. 2017, ApJ, 840, 39, doi: 10.3847/1538-4357/aa6af9
Madau, P., & Haardt, F. 2015, ApJL, 813, L8, doi: 10.1088/2041-8205/813/1/L8
Martins, F., Schaerer, D., Marques-Chaves, R., & Upadhyaya, A. 2023, A&A, 678, A159, doi: 10.1051/0004-6361/202346732
Matthee, J., Mackenzie, R., Simcoe, R. A., et al. 2023, ApJ, 950, 67, doi: 10.3847/1538-4357/acc846
May, D., Rodríguez-Ardila, A., Prieto, M. A., et al. 2018, Monthly Notices of the Royal Astronomical Society: Letters, 481, L105, doi: 10.1093/mnrasl/sly155
Menacho, V., Östlin, G., Bik, A., et al. 2019, MNRAS, 487, 3183, doi: 10.1093/mnras/stz1414
—. 2021, MNRAS, 506, 1777, doi: 10.1093/mnras/stab1491

Merloni, A., & Heinz, S. 2013, in Planets, Stars and Stellar Systems. Volume 6: Extragalactic Astronomy and Cosmology, ed. T. D. Oswalt & W. C. Keel, Vol. 6 (Springer Science), 503, doi: 10.1007/978-94-007-5609-0_11

Meynet, G., Maeder, A., Schaller, G., Schaerer, D., & Charbonnel, C. 1994, A&AS, 103, 97

Micheva, G., Oey, M. S., Jaskot, A. E., & James, B. L. 2017, ApJ, 845, 165, doi: 10.3847/1538-4357/aa830b

Micheva, G., Oey, M. S., Keenan, R. P., Jaskot, A. E., & James, B. L. 2018, ApJ, 867, 2, doi: 10.3847/1538-4357/aae372

Middleton, M. J., Heil, L., Pintore, F., Walton, D. J., & Roberts, T. P. 2015, Monthly Notices of the Royal Astronomical Society, 447, 3243, doi: 10.1093/mnras/stu2644

Morales, A. M., Finkelstein, S. L., Leung, G. C. K., et al. 2023, arXiv e-prints, arXiv:2311.04294, doi: 10.48550/arXiv.2311.04294

Nestor, D. B., Shapley, A. E., Steidel, C. C., & Siana, B. 2011, ApJ, 736, 18, doi: 10.1088/0004-637X/736/1/18

Newville, M., Stensitzki, T., Allen, D. B., et al. 2016, Lmfit: Non-Linear Least-Square Minimization and Curve-Fitting for Python, Astrophysics Source Code Library, record ascl:1606.014. http://ascl.net/1606.014

Östlin, G., Amram, P., Bergvall, N., et al. 2001, A&A, 374, 800, doi: 10.1051/0004-6361:20010832

Östlin, G., Hayes, M., Kunth, D., et al. 2009, AJ, 138, 923, doi: 10.1088/0004-6256/138/3/923

Östlin, G., Marquart, T., Cumming, R. J., et al. 2015, A&A, 583, A55, doi: 10.1051/0004-6361/201323233

Östlin, G., Rivera-Thorsen, T. E., Menacho, V., et al. 2021, ApJ, 912, 155, doi: 10.3847/1538-4357/abf1e8

Pellegrini, E. W., Oey, M. S., Winkler, P. F., et al. 2012, ApJ, 755, 40, doi: 10.1088/0004-637X/755/1/40

Prestwich, A. H., Jackson, F., Kaaret, P., et al. 2015, ApJ, 812, 166, doi: 10.1088/0004-637X/812/2/166

Prestwich, A. H., Tsantaki, M., Zezas, A., et al. 2013, ApJ, 769, 92, doi: 10.1088/0004-637X/769/2/92

Prevot, M. L., Lequeux, J., Maurice, E., Prevot, L., & Rocca-Volmerange, B. 1984, A&A, 132, 389

Rivera-Thorsen, T. E., Östlin, G., Hayes, M., & Puschnig, J. 2017, ApJ, 837, 29, doi: 10.3847/1538-4357/aa5d0a

Robertson, B. E., Ellis, R. S., Furlanetto, S. R., & Dunlop, J. S. 2015, ApJL, 802, L19, doi: 10.1088/2041-8205/802/2/L19

Ross, H. E., Dixon, K. L., Iliev, I. T., & Mellema, G. 2017, MNRAS, 468, 3785, doi: 10.1093/mnras/stx649

Savage, B. D., & Sembach, K. R. 1991, ApJ, 379, 245, doi: 10.1086/170498

Saxena, A., Bunker, A. J., Jones, G. C., et al. 2023, arXiv e-prints, arXiv:2306.04536, doi: 10.48550/arXiv.2306.04536

Sazonov, S., & Khabibullin, I. 2018, Monthly Notices of the Royal Astronomical Society, 476, 2530, doi: 10.1093/mnras/sty442

Schaerer, D., Charbonnel, C., Meynet, G., Maeder, A., & Schaller, G. 1993, A&AS, 102, 339

Schaerer, D., Izotov, Y. I., Verhamme, A., et al. 2016, A&A, 591, L8, doi: 10.1051/0004-6361/201628943

Shankar, F., & Mathur, S. 2007, ApJ, 660, 1051, doi: 10.1086/512845

Sharma, M., Theuns, T., Frenk, C., et al. 2017, MNRAS, 468, 2176, doi: 10.1093/mnras/stx578

Simmonds, C., Tacchella, S., Maseda, M., et al. 2023, MNRAS, 523, 5468, doi: 10.1093/mnras/stad1749

Sirressi, M., Adamo, A., Hayes, M., et al. 2022, MNRAS, 510, 4819, doi: 10.1093/mnras/stab3774

Smith, B. M., Windhorst, R. A., Cohen, S. H., et al. 2020, ApJ, 897, 41, doi: 10.3847/1538-4357/ab8811

Soderblom, D. R. 2021, in COS Data Handbook v. 5.0, Vol. 5 (STScI), 5

Swartz, D. A., Soria, R., Tennant, A. F., & Yukita, M. 2011, The Astrophysical Journal, 741, 49, doi: 10.1088/0004-637x/741/1/49

Topping, M. W., Stark, D. P., Endsley, R., et al. 2023, arXiv e-prints, arXiv:2307.08835, doi: 10.48550/arXiv.2307.08835

Verhamme, A., Orlitová, I., Schaerer, D., & Hayes, M. 2015, A&A, 578, A7, doi: 10.1051/0004-6361/201423978

Verhamme, A., Orlitová, I., Schaerer, D., et al. 2017, A&A, 597, A13, doi: 10.1051/0004-6361/201629264

Vink, J. S., de Koter, A., & Lamers, H. J. G. L. M. 2001, A&A, 369, 574, doi: 10.1051/0004-6361:20010127

Vinokurov, A., Fabrika, S., & Atapin, K. 2013, Astrophysical Bulletin, 68, 139, doi: 10.1134/S1990341313020028

Volonteri, M., & Gnedin, N. Y. 2009, ApJ, 703, 2113, doi: 10.1088/0004-637X/703/2/2113

Wang, B., Heckman, T. M., Amorín, R., et al. 2021, ApJ, 916, 3, doi: 10.3847/1538-4357/ac0434

Wofford, A., Sixtos, A., Charlot, S., et al. 2023, MNRAS, 523, 3949, doi: 10.1093/mnras/stad1622

Yeh, J. Y. C., Smith, A., Kannan, R., et al. 2023, MNRAS, 520, 2757, doi: 10.1093/mnras/stad210

Zackrisson, E., Rydberg, C.-E., Schaerer, D., Östlin, G., & Tuli, M. 2011, ApJ, 740, 13, doi: 10.1088/0004-637X/740/1/13

Zastrow, J., Oey, M. S., Veilleux, S., & McDonald, M. 2013, ApJ, 779, 76, doi: 10.1088/0004-637X/779/1/76

Zastrow, J., Oey, M. S., Veilleux, S., McDonald, M., & Martin, C. L. 2011, ApJL, 741, L17, doi: 10.1088/2041-8205/741/1/L17